Energy dissipation in granular materials in DEM simulations

RECTOR AHURA MUKWIRI

Energy dissipation in granular materials in DEM simulations

Rector Ahura Mukwiri

Thesis submitted towards the
degree of MSc by Research

Department of Engineering
Durham University
United Kingdom

March 2022

Rector Ahura Mukwiri

Abstract

Soil has generally been treated as a continuum from as early as the eighteenth century. Since then the analysis of soil behaviour in practical engineering analyses and development of constitutive models has depended on a continuum assumption. However, in order to gain a deeper understanding of the behaviour of soils and their particulate nature, there is a need to move from continuum mechanics to discrete models. Such modelling is possible using the Discrete Element Method (DEM). In this thesis an open source DEM particle simulation software, LIGGGHTS is used to study the relationships between grain scale parameters and energy dissipation in granular media in one-dimensional compression. In order to measure the dissipated energy, changes in energy terms are traced at every time step and the principle of energy conservation applied. The influence of particle size distribution, initial void ratio, and inter-particle friction coefficient on energy dissipation are studied and discussed. It is shown that increasing the coefficient of uniformity decreases the energy dissipated; lowering the initial voids ratio results in steeper energy dissipation curves; and a higher inter-particle coefficient of friction yields more energy dissipation. It is hoped that the knowledge gained of the relationship between grain scale parameters and energy dissipation can be built upon to formulate constitutive relationships within the hyperplasticity framework. It is envisioned that relating grain scale parameters to constitutive models will allow the formulation of models that are purely based on the micro-mechanics of granular media.

Declaration

The work in this thesis is based on research carried out in the Computational Mechanics Group, Department of Engineering, Durham University. No part of this report has been submitted elsewhere for any other degree or qualification and it is all my own work unless referenced to the contrary in the text. Parts of this work have been published in the following:

Conferences

Mukwiri, R.A., Ghaffari Motlagh, Y., Coombs, W.M. & Augarde, C.E. (2017), Grain scale parameters in dissipative driven constitutive models, International Conference on Particle-Based Methods (PARTICLES) - V International Conference on Particle-Based Methods: fundamentals and applications (PARTICLES 2017), Hannover, 26-28 October, 2017, 504-513

Mukwiri, R.A., Ghaffari Motlagh, Y., Coombs, W.M. & Augarde, C.E. (2017), Energy dissipation in granular materials in triaxial tests, in Faramarzi, A. & Dirar, S. eds, 25th UKACM Conference on Computational Mechanics. Birmingham, UK, University of Birmingham, 191-194.

Mukwiri, R.A., Ghaffari Motlagh, Y., Coombs, W.M. & Augarde, C.E. (2016), Energy dissipation in granular material under 1D compression, ACME - UK 2016 24th Conference of the Association for Computational Mechanics in Engineering. Cardiff, UK, Cardiff University, Cardiff, 231-234.

Contents

List of Figures

List of Tables

List of Algorithms

Chapter 1

Introduction

Soil analysis is an important step in geotechnical engineering to determine the quality of soil. This knowledge can be used to determine the suitability of soil for a construction. Samples of soil can be taken to soil laboratories where tests are carried out such as compression tests, compaction tests, moisture content tests, Atterberg limit tests. The properties from such tests can be used in engineering design.

Soil has generally been treated as a continuum from as early as the eighteenth century [5]. This assumption has since been used in engineering design for practical purposes. Indeed many constitutive models are built on this assumption. However, using a method of modelling soils as discrete particles can facilitate understanding soil better. Such a method is the Discrete Element Method (DEM) originally introduced by Cundall and Strack [6].

The DEM is a particle scale modelling technique that involves procedures for simulating the complete behaviour of systems of discrete, interacting bodies [7]. The origin of DEM can be traced back to the work of Cundall and Strack [6]. The development of the DEM was to accurately capture the internal behaviour of granular media. Some of the grain scale behaviour of materials like localised stresses, or the interactions at grain scale levels are hard to observe using laboratory experiments. Recently, however, CT and X-Ray scans have been used to observe grain scale properties and behaviour (for example, [8]). The scope of DEM used in this thesis was at the time of its development envisioned to provide a simple way to analyse granular matter.

Cundall and Strack [9] stated that a similar model at the time to DEM was from the works of Rodriguez-Ortiz [10] where the finite element method was used to model assemblies of discs. A stiffness matrix was constructed by taking into account the geometry of the particles and the current stiffness of each contact. An inversion of this matrix would then gave the incremental displacements given the last known forces. An iterative approach was taken to deal with the slip at contacts. The stiffness matrix is updated whenever a new contact is formed or broken. All particles communicate with each other at every solution step.

In contrast to the above described method, the DEM is an explicit approach by considering the individual particles and their interactions without employing the finite element method to update particle positions as detailed in [6]. The time step should be chosen to be small enough so that disturbances of each particle cannot propagate beyond its neighbouring particles in each time step. The resultant forces for each particle are then calculated by only considering the particles in contact.

The validity of the DEM was shown by making comparisons of its predicted results with experiments. Cundall and Strack [6] conducted a numerical reproduction of a test on photostatic discs reported in 1969 by de Josselin de Jong and Verruijt [11]. There was good agreement between the contact forces predicted

by the DEM and those observed in the experiment.

To demonstrate the application of the DEM, further stress-controlled boundary simulations of 100 and 1000 discs were conducted and both the internal and boundary behaviour were observed by Cundall and Strack [9]. It was found that the predictions from these simulations provided understanding of granular media. These observations together with the validations above led Cundall and Strack to say that "the distinct element method is a valid method for modelling assemblies of discrete particles" and "it can be used with confidence even in situations when it is not possible to do a corresponding physical test" [9].

Unlike continuum-based materials modelling, DEM does not require a material constitutive model. On the contrary, Cundall and Strack [9] hoped that the method will provide a framework from which constitutive models can emerge from the results of simulations using the method. Many DEM related papers have indeed shown that the constitutive models can be derived from DEM results [12].

The DEM method in this thesis is used to investigate grain scale parameters in relation to energy dissipation, a core component of the hyperplasticity approach to constitutive modelling [13]. The hyperplasticity approach allows the constitutive behaviour of a material to be derived from a free-energy function and a dissipation rate function [13]. This approach stems from the works of Ziegler [14] and Houlsby [15]. Once these scalar functions have been specified, the yield function, flow rule and the stress and strain relationships can be derived without need of any additional assumptions. The first scalar function is derived from the First law of Thermodynamics and the dissipation function is a consequence of the Second law of Thermodynamics.

By understanding the fundamental causes of energy dissipation in a DEM simulation, a dissipation function could potentially be formulated leading to a constitutive relationship formulation directly informed by physical measurements at a particle level. In this thesis, one-dimension normal compression simulations are used to understand granular mater. One-dimensional normal compression tests have been used in the past to investigate granular behaviour such as compressibility and the evolution of the particle size distribution using both physical tests and Discrete Element Method (DEM) simulations (see for example [16–19]). The present study used the DEM to conduct one-dimensional normal compression tests to study energy dissipation in granular media without particle breakage. The grain scale parameters explored are: the inter-particle friction coefficient, particle size distribution and the initial void ratio. The relationship between these parameters and energy dissipation are discussed. It is envisioned that the findings can help inform the formation of continuum functions linking energy dissipation to grain scale parameters.

There are a number of commercial and open source DEM software currently in use for the study of particulates (e.g EDEM, Newton, ESyS, PFC, LIGGGHTS, etc [20–24]). The simulations presented in this thesis were conducted using the open source LIGGGHTS software developed by Kloss et al. [25]. This software offers extensive development for granular media studies. It also provides the user an opportunity to extend the code to their personal interests that may not yet be available in the open source code. It was therefore seen as an attractive tool for the simulations in this thesis.

The remainder of this thesis is divided into the following chapters:

- Chapter 2 is concerned with providing DEM details including: the DEM model description and a literature review of how the DEM has been used.
- Chapter 3 discusses the one-dimensional normal compression test simulations that were carried out by the author. The relationship between the inter-particle friction coefficient, particle size distribution and the initial void ratio and energy dissipation are discussed.
- Chapter 4 draws conclusions from the thesis and suggests some future work options.

Chapter 2

Discrete element modelling

The purpose of this chapter is to explore the use of the DEM and its relevance to energy dissipation studies. Section 2.1 will describe the DEM. Section 2.2 will provide applications of the method in general, and specific to energy dissipation. The process followed in the LIGGHTS software used for the simulations in this thesis will be described in Section 2.3 before the chapter is concluded in Section 2.4.

2.1 The DEM model

The calculations involved in a DEM simulation follow the sequence outlined in Figure 2.1. At the start of the simulation, the user inputs the system geometry and the contact model information that will be used. At each time step of the simulation, contacting particles are identified and contact forces calculated based on particle overlaps and stiffnesses at contacts. The resultant force acting on each particle including the body and external forces is then calculated. From this resultant force, the particle acceleration is calculated and then integrated to get the velocities. With these velocities, particle displacement and rotation are then calculated and the particle positions updated. The simulation time is then increased by one time step while updating boundary positions as required. Depending on the purpose of the simulation, data can be output at any stage of the simulation cycle.

At each stage of the DEM simulation, each particle will have two types of motion: translational and rotational. These motions are influenced by the interactions the particle has with other particles, fluid surrounding it, and any bounding walls. Such interactions make this problem complex to solve analytically. In DEM, as mentioned in Chapter 1, a time step is chosen such that the resultant forces on each particle can be calculated exclusively from the interactions with both contacting forces and surrounding fluid (see Section 2.1.3). If the simulation involves powders like clay particles, other non contacting forces such as van der Waals can be included. From Newton's second law of motion the governing equations for particle i with mass m_i and moment of inertia I_i describing the translational and rotational motion can be written as

$$m_i \frac{\mathrm{d}\mathbf{v}_i}{\mathrm{d}t} = \sum_j \mathbf{F}_{ij}^c + \sum_k \mathbf{F}_{ij}^{nc} + \mathbf{F}_i^f + \mathbf{F}_i^g, \tag{2.1}$$

$$I_i \frac{\mathrm{d}\boldsymbol{\omega}_i}{\mathrm{d}t} = \sum_j \mathbf{M}_{ij}, \tag{2.2}$$

where $\mathbf{v}_i$ and $\boldsymbol{\omega}_i$ are the particle translational and rotational velocities respectively, $\mathbf{F}_{ij}^c$ and $\mathbf{M}_{ij}$ are the contact force and torque acting on the particle i by particle or wall j, $\mathbf{F}_{ij}^{nc}$ is the non contacting

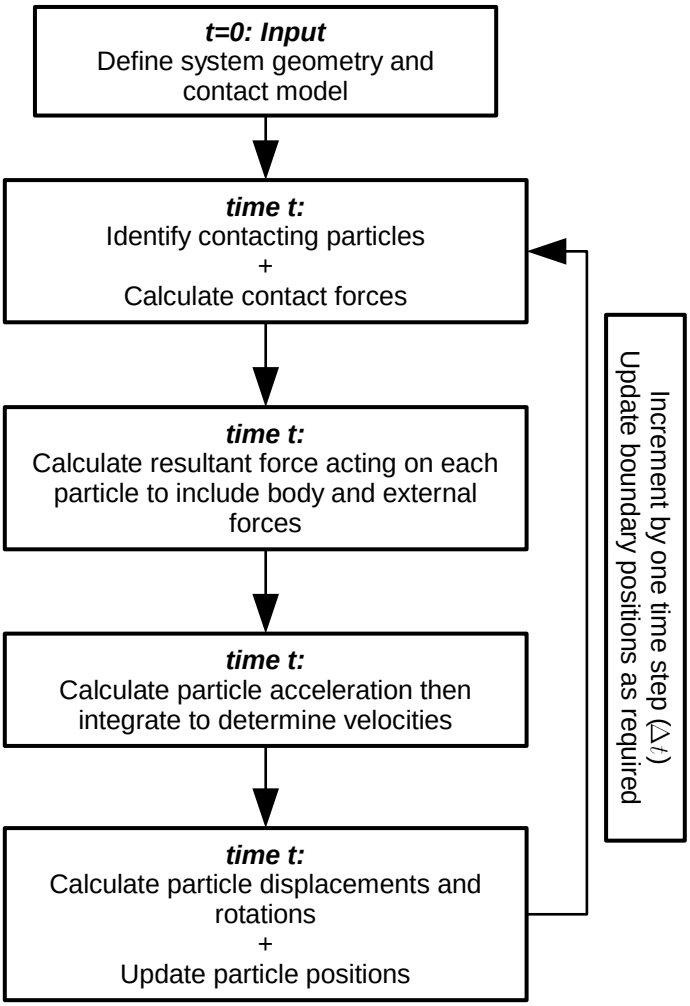

Figure 2.1: Schematic diagram of DEM simulation calculations (adapted from [1])

force like an attraction force in powders from source k acting on particle i, $\mathbf{F}_i^g$ is the gravitational force, and if a fluid interaction is considered, then, $\mathbf{F}_i^f$ is the particle-fluid interaction force on particle i. The translational acceleration, $\frac{\mathrm{d}\mathbf{v}_i}{\mathrm{d}t}$ and rotational accelerations, $\frac{\mathrm{d}\boldsymbol{\omega}_i}{\mathrm{d}t}$ are derived from 2.1 and 2.2 respectively. The translational and rotational velocities are then derived by integrating these accelerations respectively. The particle displacement and rotation are then obtained by integrating these velocities.

A crucial part of the DEM simulation is identifying particle contacts and calculating contact forces. Sutmann [26] observed that these calculations can take up 90% of the simulation. Section 2.1.2 discusses various contact force models that are typically considered.

The first stage in a DEM simulation is sample preparation. In this stage, the geometry of interest is defined and particles are generated. Governing contact models are also selected at this stage of the simulation. As will be discussed in Section 2.1.1, particle generation can take a significant amount of time if not carefully executed. Some of the methods used for this stage are discussed next in Section 2.1.1.

2.1.1 Initial geometry and specimen generation

The first step in a DEM simulation, as shown in Figure 2.1, is to define the system geometry and populate it with particles. This step is analogous to the mesh generation stage involved in a conventional

continuum analysis. In DEM simulations, particle generation can easily take as long as the remainder of the simulation, and in some cases can be longer depending on the method used.

Just like in laboratory experiments, specimen preparation is very crucial to the DEM simulation. It defines the initial conditions that will influence the simulation behaviour. This stage is not necessarily entirely done within the dedicated DEM software of choice. The researcher can simply import the initial particle configuration into the DEM software and initiate the simulation with it. If the researcher wishes, this process can be carried out in the DEM software used for the rest of the analysis. There is no clear agreement as to the best method to use for sample preparation and as such, the variety of methods typically used will be discussed.

O'Sullivan [1] provides a detailed discussion of the various methods used in sample preparation including boundary conditions adopted. For a deeper understanding of boundary conditions and sample preparation methods explained below the interested reader is referred to [1]. The next Section will discuss boundary conditions.

Boundary conditions

Boundary conditions are equally important in DEM simulations as they are in continuum simulation. These are specified by introducing boundaries that enclose the simulation space. There are four commonly used boundaries in DEM simulations; rigid walls, periodic, membrane, and axisymmetrical. Rigid, periodic, and membrane boundary examples are shown in Figure 2.2. The simulations presented in the present thesis used rigid walls.

Rigid walls boundaries involve enclosing the simulation space with a rigid line (in 2D) or surface (in 3D). The surface can either be a mesh inserted into the DEM code or fixed defined planes. In some cases, a set of particles could be used to define the wall such that these particles form a rough surface for the particle-wall contacts. The movement of the wall can be displacement controlled by applying a velocity to it such that a desired effect on the particles is achieved (such as a target void ratio, a target internal stress state, a target axial strain, among others). An indirect application of a wall velocity is effected when servo-controlled rigid walls are used. Here the pressure exerted on the wall surface or an internal stress is monitored and compared to the target wall stress desired. If this is greater or less than the target stress within a specified tolerance, the wall velocity is adjusted to bring the wall stress to the desired target. The wall velocity is set to zero if the monitored stress state is within tolerance.

Rigid boundaries can sometimes be used to add inclusions in the sample. Kinloch and O'Sullivan [27], for example, modelled pile installation and cone penetration testing using rigid boundaries. These boundaries are only used to update particle coordinates since they have no inertia. They are, therefore, similar to displacement boundary conditions in continuum analyses.

Some of the effects of using rigid boundaries such as the underestimation of small-strain stiffness and the effect on the force network are discussed by Marketos and Bolton [28]. Other research presents limitations on the use of rigid boundaries such inconsistent void ratio values between particles around boundaries and those further away (e.g. [29, 30]), which should be taken into account when this boundary method is used.

Periodic boundaries can be used in DEM simulations to eliminated rigid boundary effects [31]. A representative cell block is repeated infinitely in all directions. Only the representative cell is specified in the simulation and, therefore, its size should be carefully considered. When a particle approaches boundaries, it begins to re-enter at the opposite boundary, which means that each particle is not restricted to only contact adjacent particles. Strains can be applied to the periodic boundaries to model increase or decrease in internal stresses. In this case, the entire representative cell stress would be monitored to

adjust the strain rate.

Flexible boundaries can be used to represent the flexible latex membrane used in triaxial tests and other similar boundaries. There are two common approaches used. Both approaches model the outermost particles as membrane particles. One approach inserts flexible contact springs with a high tensile capacity to link the outermost particles and then a force is applied to these particles to reach the desired confining pressure on the membrane (e.g. [32, 33]). Another approach involves applying this force to the membrane particles without any special links between these membrane particles (e.g. [34]).

An interesting study by Cheung and O'Sullivan [35] showed a comparison between rigid and flexible membrane boundaries. By comparing the boundary stresses of both methods, they observed that the macro-scale response was not sensitive to the boundary condition used during the simulation. Differences, however, were observed in the internal material deformation response by looking at the specimen particle rotations. The observations seen in a typical laboratory triaxial test were captured by the flexible membrane.

To save on computational cost, a combination of the above boundary conditions can be used to simulate different parts of the system under study. If a system is axisymmetrical, only a part of the domain is sufficient to define the system. This is regularly done in finite element modelling of continuum problems. This concept has also been employed in the DEM. Cui et al. [36], for example proposed circumferential periodic boundaries symmetrical about the z axis that only model a slice of the problem whose pattern repeats in the x and y axis.

Once a boundary condition has been defined, the particles can then be inserted into the system. There are a number of methods that can be employed to this effect and some of these methods will be discussed in the following section.

Random particle generation

One of the most commonly employed methods of sample preparation is the random particle generation method. To achieve this, programming languages or mathematical software like Matlab, C, C++, python, Fortran, are typically used. This can, for example, be achieved by generating seeds through repeated calls to specific random number generation functions. Each particle would then receive unique numbers attached to it defining it's coordinates. Sometimes some sets of numbers may not be unique and, therefore, care must be taken when generating these numbers. Each particle would then be associated to a set of random numbers, for example, a spherical particle would have an x, y and z coordinates plus an extra number for the radius. These random numbers are usually between 0 and 1. Scaling and translation can be done to the coordinates as desired. Based on the extent of the particle, some overlaps can be generated on subsequent function calls. These can be resolved by translating the particle to an open space.

If a specific particle size distribution is desired, large particles can be generated first and then smaller particles next as illustrated in Figure 2.3. For example, Ferrez [37] placed large spherical particles in a cylinder and added smaller particles to achieve a dense sample on subsequent iterations each iteration adding smaller ones than the previous.

When matching particle size distributions to the physical observations, very small particles are usually ignored in Geomechanics DEM simulations. One of the reasons for ignoring this is because the time step size is proprtional to the ratio $\sqrt{m/K}$ where m is the particle mass and K the effective contact stiffness [1]. The smaller the particle mass, therefore, the smaller the time step required for a stable simulation. Another reason why very small particles are typically ignored in the DEM simulations is because they tend not contribute to the strong force network, that is, they tend to be unnecessary in supporting the structure. Potyondy and Cundall [38] for example, described a process that eliminated non contacting

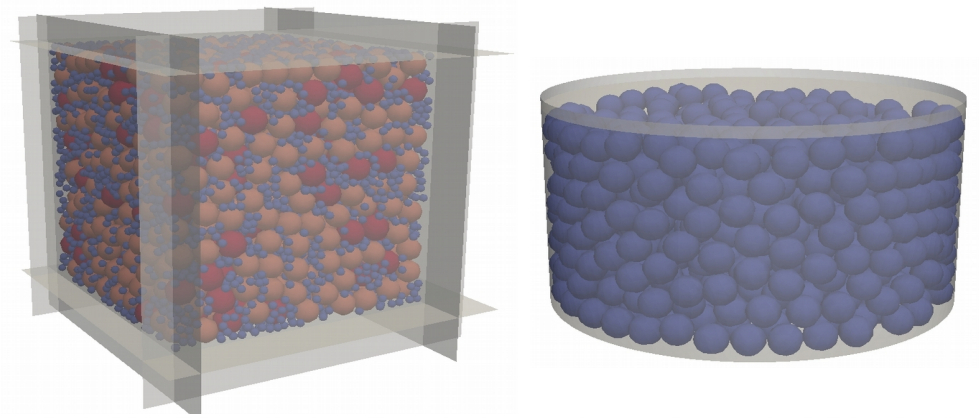

(a): Examples of fixed boundaries. Boundaries can be meshes or invisible planes or lines

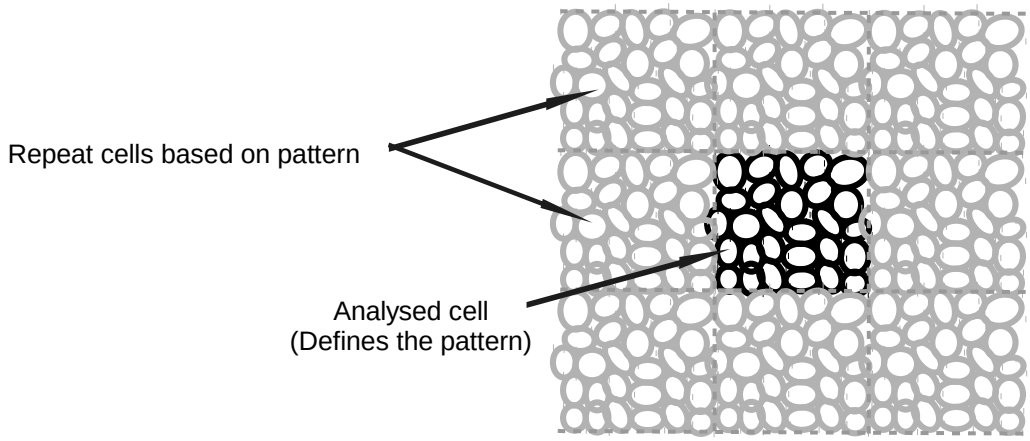

(b): An illustration of a periodic boundaries using a square cell repeat pattern

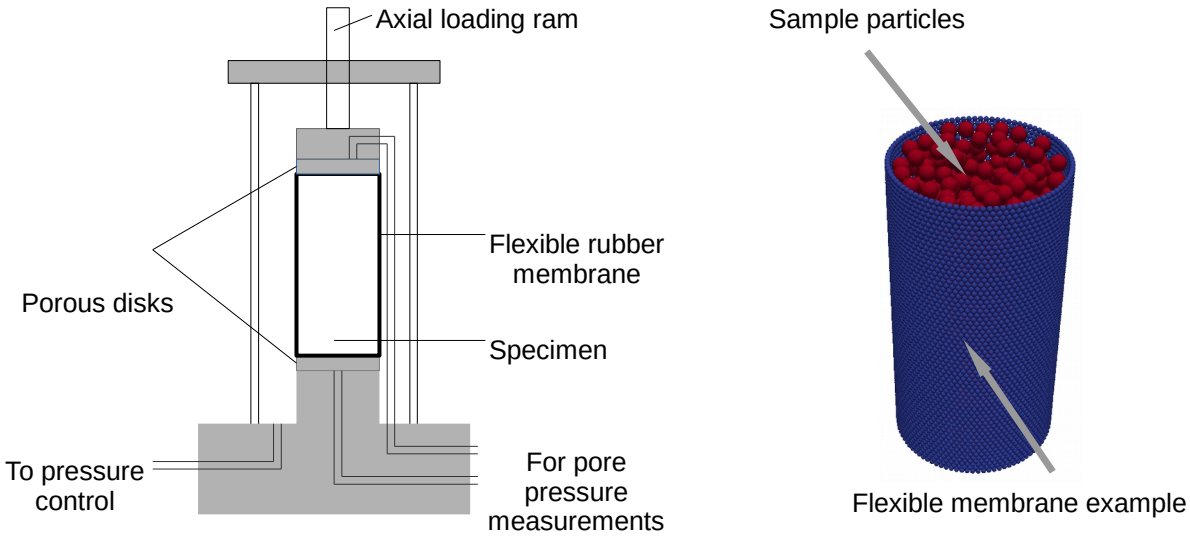

(C): Flexible membrane: (Left) Triaxial test apparatus; and (Right) DEM example of a flexible membrane made up of small particles

Figure 2.2: DEM Boundaries. (b) is adapted from [1] while the rest are either drawn by the author or are snapshots from the author's simulations.

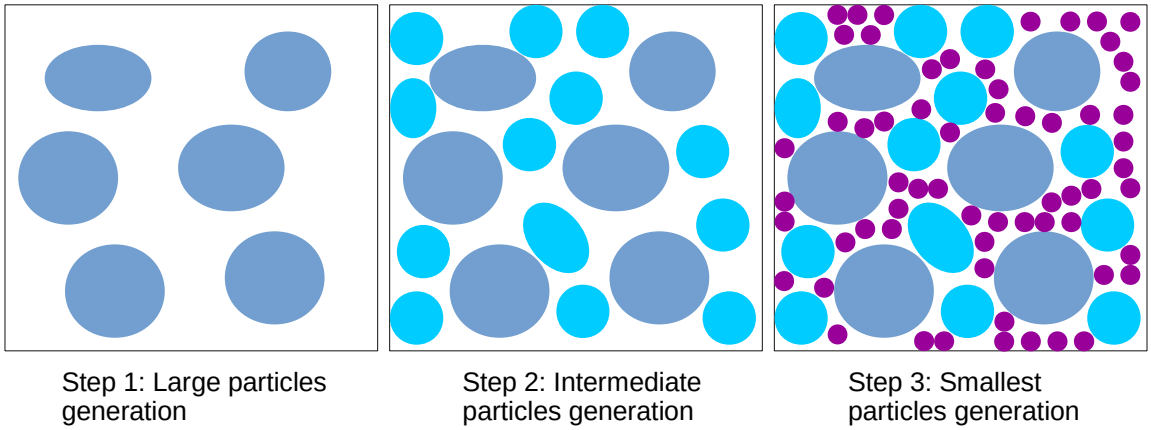

Figure 2.3: Illustration of psd matching random particle generation process. Particles can take on different shapes depending on the study. Adapted from [1].

particles which they called floaters. However, when a significant percentage of small particles is present in the sample, it will contribute to the strong force network and would therefore be included in the sample. Minh et al. [39] found that a 30% silt particle contribution was required for small particles to feature in the strong force network formation.

The density of randomly placed particles can be increased by compressing the bounding walls or applying a compressive strain to the boundary particles if periodic boundaries are used. This can be done over several time steps until a target stress state is reached or a specified void ratio is achieved. However, the author's experience has shown that increasing the sample density using this method can be time-consuming. This is because the wall or boundary movements have to be small enough to prevent large particle accelerations that would result in an unstable system. To reduce the simulation time, the method could use a wall velocity or strain rate that is initially high and keep reducing it at subsequent steps until the target initial conditions are achieved. An even better approach would be using an alternative method that involves particle size growth.

In the particle size growth method, used for example in LIGGGTS [24], randomly generated particles are grown over several time steps. For spherical or circular particles, this is achieved by growing the radius of each particle. Typically, the growth mechanism is done for every particle at each growth step. A constant rate can be chosen to achieve the desired goal. A better alternative to the constant rate is a variable growth rate such that the rate of particle growth reduces at subsequent growth steps. A constant rate of growth would need to be very small in order to maintain system stability when contacts start to form. The rate of particle growth in a system of spherical or circular particles can be set by multiplying the radii by a growth factor.

When growing the particles in size, contacts will be formed. At this stage, particle overlaps may be introduced. The growth would be paused for particles over several time steps for the particles to regain a system of equilibrium where there are no particle overlaps as illustrated in Figure 2.4. During these non-growth steps, a series of calculations to bring the system to equilibrium are made to ensure that subsequent growth steps do not generate excessive accelerations by generating large particle overlaps, which would result in very large accelerations.

At the completion of the particle size growth process, the system should again be brought to a state of equilibrium. The criteria for equilibrium can be based on the resultant force or on the stress state of the sample. The maximum ratio of the resultant force to the particle mass can be monitored and equilibrium

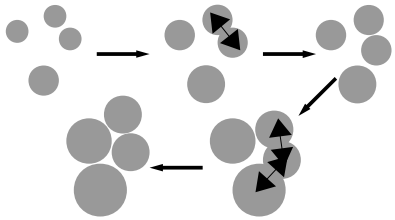

Figure 2.4: Illustration of particle radii growth (adapted from [1])

is reached when the maximum ratio is smaller than a pre-set value. The stress state can alternatively or additionally be used to judge equilibrium by monitoring it until it reaches a constant value within a specified tolerance. An alternative or addition to these methods would be monitoring the total number of contacts until they reach a constant value.

There are other approaches similar to the particle expansion approach described above. One such approach is a lily pond method described by Bagi [40] where randomly created points are each grown in size as disks or spheres until another particle is touched at which point the expansion ceases.

An interesting method of particle generation that uses random points is an under-compaction method by Jiang et al.[2] illustrated in Figure 2.5. This method involves generating particles randomly in layers. The first layer is generated and then compacted to a void ratio e_1. The bounding box is then extended and another layer of particles is randomly generated in free space. This layer is then also compacted to now a void ratio e_2. The process is repeated until the target height is achieved. The void ratios are such that $e_1 > e_2 > ... > e_j > .... > e_{target}$.

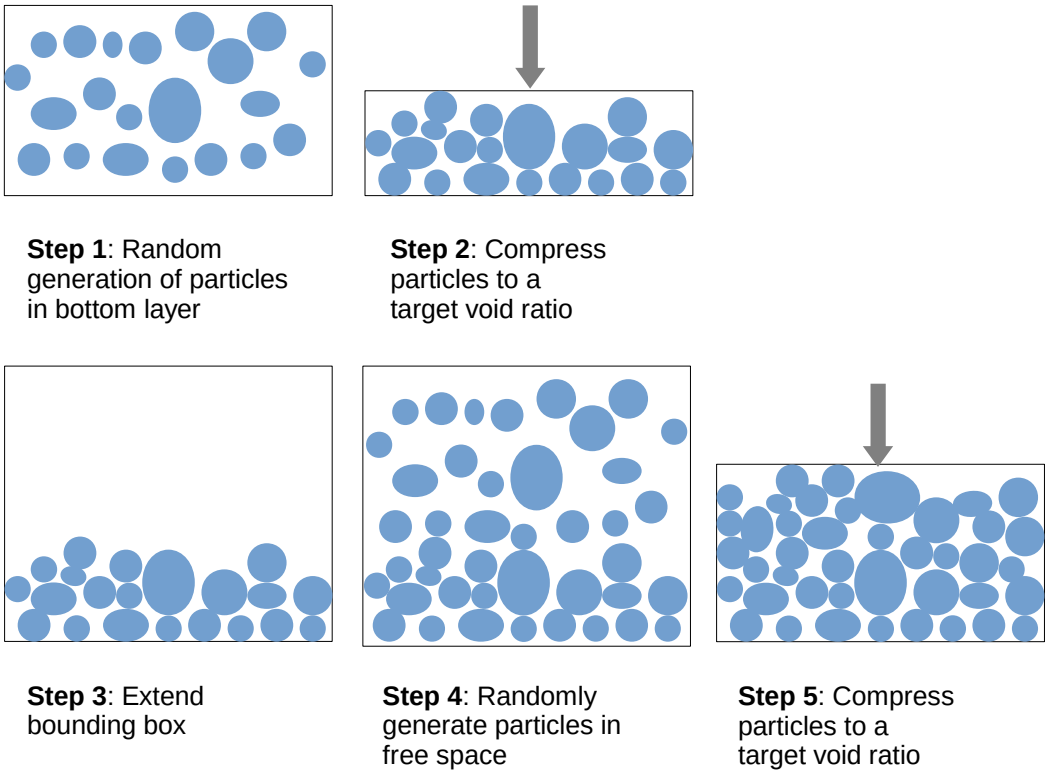

Figure 2.5: Illustration of an under-compression method by Jiang et al. [2]

Other particle generation methods

In nature, gravitation has a big part in the movement of particles. This can be modelled in the sample preparation stage in the DEM by using a gravitation or sedimentation method such that particles are allowed to settle under gravity. For example, Abbiready and Clayton [41] generated non-overlapping particles at specific vertical levels but random horizontal positions, and then applied a gravitation force to particles to allow them to settle.

Ciantia et.al [42] developed a simple and very efficient periodic cell-replication method (PCRM) for generating particles. In the PCRM, a periodic cell is first generated where the particles in the cell match the desired particle-size distribution and are sufficient for the cell to be a representative element volume. The cell is then equilibrated at the desired porosity, stress state and coordination number. It is then replicated to fill the problem domain, which is then equilibrated to form a homogeneous sample with the desired initial state. Ciantia et.al [42] compared the PCRM to sedimentation method and found the PCRM to be significantly more efficient.

Once a particle specimen is generated (or even during particle generation), contact laws to govern particle contacts are specified. These are the subject of the next section.

2.1.2 Contact Laws

A particle contact does not generally happen at a single point, but rather over a finite area as a result of particle deformation. This area in DEM is modelled as an overlap between the contacting particles. A contact plane can be visualised in this area on which a normal force, and a tangential force act. For spherical or disc particles, the contact will look like the illustration in Figure 2.6. This is an idealised view of the particle contact that is often employed in DEM simulations to help reduce computational costs.

As illustrated in Figure 2.6(b), rheological models are used to describe the normal and tangential contact forces. In the figure, linear springs, dashpots and joints model contacts in normal and tangential directions and frictional slider in tangential direction [3]. These models can either be linear or non-linear and are the basis on which the contact constitutive relationships have been developed to calculate the normal and tangential contact forces.

Normal contact force models

Linear contact models are generally the most simple models. For a simple linear elastic springs model, normal force is calculated as:

$$F_n = K_n \delta_n, \tag{2.3}$$

where K_n is the contact stiffness in the normal direction with the units of N/mm, and δ_n is the overlap at the contact point normal to the contact. This type of contact model would only be used to minimise the overlap distance at the contact.

The most commonly used linear model was proposed in the 1979 work of Cundall and Strack [6] in which a spring-dashpot model was used such that the spring modelled elastic deformation and the dashpot accounted for the viscous dissipation. The force-displacement relationship is given by

$$F_n = K_n \delta_n + C_n \dot{\delta}_n \tag{2.4}$$

where C_n is the non-linear dissipative term. Delaney et al. [43] proposed that contact energy dissipation

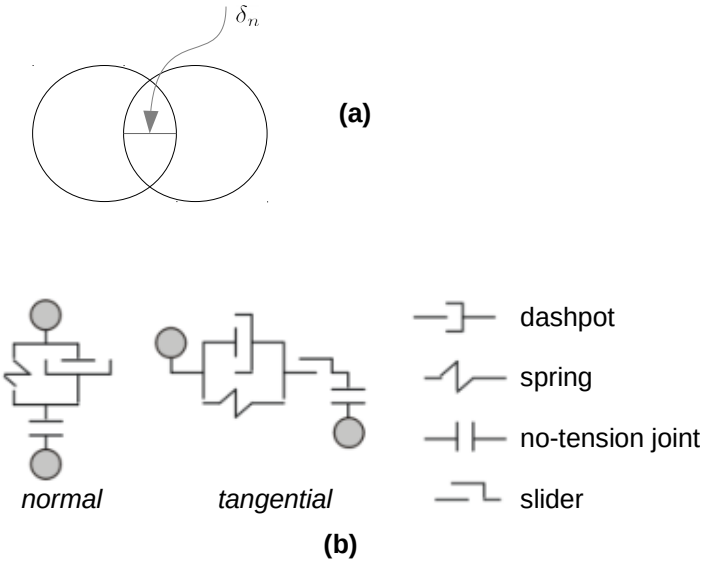

Figure 2.6: Illustration of DEM particle contact using spheres or discs: (a) normal displacement; (b) rheological models examples from [3]

was related to velocity and argued that at high impact velocities there is less energy dissipated. Their dashpot term was therefore dependant on the impact velocity.

Hertz-Mindlin and Deresiewicz contact model (often abbreviated as Hertz-Mindlin) is another commonly used model in the DEM. [44, 45] are often cited as the original papers on which this model is based with the work of Hertz's (1882) describing the normal contact behaviour while the work of Mindlin and Deresiewicz (1953) describes the tangential contact. Tangential contact models are described below. The work of Johnson [46] can help understand Hertz's (1882) work since the original paper was published in German. For small and elastic deformations, the normal contact force is given as

$$F_n = \underbrace{\left(\frac{2G^* \sqrt{2R^*}}{3(1-\nu^*)} \sqrt{\delta_n} \right)}_{K_n} \delta_n, \tag{2.5}$$

where $(.)^*$ denotes the equivalent quantity of two particles (A and B) are in contact such that the shear modulus $G^* = 0.5(G^A + G^B)$, the particle radius $R^* = (2R^A R^B)/(R^A + R^B)$ and Poisson's ratio $\nu^* = 0.5(\nu^A + \nu^B)$. The particle-wall contact equivalent values are equal to those of the particle.

To account for energy dissipation on in the Hertz-Mindlin, extra terms are included in the calculation of the normal contact force. In the LIGGGHTS software DEM code [25], for example, the contact normal for the Hertz-Mindlin model is calculated as

$$F_n = K_n \delta_n - \gamma_n v_{AB} \tag{2.6}$$

where the normal stiffness K_n is calculated as in Equation (2.5), v_{AB} is the relative velocity of particles A and B in contact, and $\gamma_n \geq 0$ is the viscoelastic damping constant.

Walton and Braun [47] introduced a latching-spring model that describes the normal force. Their

linear contact model behaves differently if loading or unloading such that

$$\begin{aligned} F_n &= K_{1,n}\delta_n \qquad\qquad \text{(if loading)} \\ F_n &= K_{2,n}(\delta_n - \delta_n^0) \quad \text{(if unloading)} \end{aligned} \tag{2.7}$$

where $K_{1,n}$ and $K_{2,n}$ are the spring stiffness terms in the normal direction, and $\delta_n^0 = F_n^{max}/K_{2,n}$, where F_n^{max} is the maximum normal contact force reached before unloading. The spring stiffness values are user-specified such that $K_{2,n} > K_{1,n}$. Alternatively, $K_{2,n}$ can be set as a function of the maximum normal force and $K_{1,n}$, i.e. $K_{2,n} = K_{1,n} + SF_n^{max}$ where S is a constant.

The Walton-Braun model dissipates energy through the loss of kinetic energy in every collision. This energy loss is quantified by the coefficient of restitution, e, which is equal to 1 if there is no energy loss in a perfect collision, but less than 1 in typical collisions. Given two particles A and B with velocities in the normal direction v_n^A and v_n^B before collision, and $v_n^{'A}$ and $v_n^{'B}$ after collision respectively, it follows that the coefficient of restitution is

$$e = \frac{v_n^{'B} - v_n^{'A}}{v_n^B - v_n^A}. \tag{2.8}$$

During loading, the kinetic energy is converted to strain energy and on unloading, the strain energy is transferred to kinetic energy.

There are many other normal contact forces not mentioned here. There is however, some interesting reviews that can be very useful to the reader. Ye and Zeng [48] provided a useful review of many normal contact force models. Thornton et al. (2017) [49] carried out a review of the normal contact force models used for adhesive and non-adhesive contacts, where adhesive here refers to the presence of bonds such as cohesion, van der Waals forces, electrostatic forces. Their work is useful in understanding the limitations of different normal contact force models with adhesion as the focus.

Tangential contact force models

The contact force component that acts on the surface of the particle in contact is often referred to as either the tangential force or shear force. This force acts during and before sliding for contacting particles. Initiation of sliding can be modelled by considering the Coulomb frictional model which includes the coefficient of friction μ at contact in the calculations. Given the normal contact force F_n, the tangential force F_t is truncated as $|F_t| \leq \mu F_n$. Once $|F_t| = \mu F_n$ then sliding is initiated. If cohesion is included in the DEM simulation, then a cohesion term c is added to the truncation such that $|F_t| \leq \mu F_n + c$. As with the normal contact force, there are many tangential contact fore models that can be used to calculate F_t.

Cundall and Strack [6] had a simple calculation of the tangential force given by

$$F_t = K_t\delta_t - C_t\dot{\delta}_t \text{ and } |F_t| \leq \mu F_n + c, \tag{2.9}$$

where K_t is a user-specified tangential stiffness, δ_t the tangential displacement, C_t is a user-specified damping term in the tangential direction, and $\dot{\delta}_t$ the rate of change of the tangential displacement. Cohesion c is also a user-specified where attraction between particles exists.

One of the earliest developed tangential contact force models is from the experimental work of Mindlin and Deresiewicz (1953) [45]. Their work proposed that the tangential force-displacement relationship is dependant on the current normal force, the complete load history, and the instantaneous change in the normal and tangential contact forces. A description of this model can be found in [50, 51].

Thornton and Yin (1991) [52] was developed a tangential contact non-adhesive model based on the

experimental work of Mindlin and Deresiewicz (1953). The tangential stiffness in this model is given as

$$K_t = 8G^*\theta\delta_n \pm \mu(1-\theta)\frac{\Delta F_n}{\Delta\delta_t} \tag{2.10}$$

where the negative sign is used during unloading and Δ indicates a change over the load step. Expressions for parameter θ were given depending on whether the equation is used during loading, unloading or reloading (refer to [1, 52]).

Walton and Braun [47] also proposed a tangential contact model that was a simplification of the experimental work of Mindlin and Deresiewicz (1953). In their model, the tangential stiffness matrix was given by

$$\begin{aligned} K_t &= K_0\left(1-\frac{F_t - F_t^*}{\mu F_n - F_t^*}\right)^{\Gamma} \text{ for slip when loading or reloading as } F_t \text{ increases} \\ K_t &= K_0\left(1-\frac{F_t^* - F_t{}^{\Gamma}}{\mu F_n + F_t^*}\right) \text{ for slip when unloading as } F_t \text{ decreases} \end{aligned} \tag{2.11}$$

where K_0 is the initial tangential stiffness, and Γ is a constant parameter that usually has the value $1/3$ to agree with Mindlin's theory. F_t^* is initially set to zero and updated to equal the tangential force, F_t, whenever the slip direction is reversed. It is also dependant on the loading history. Subsequently, the new tangential force $F_t{}'$ for the next time step is updated as

$$F_t{}' = F_t + K_t\delta_t. \tag{2.12}$$

Contact detection

The focus above has been on contact resolution. But the first step required before these forces are calculated is contact detection, which will now be discussed. There is a variety of approaches that have been developed in achieving efficient algorithms to search for contacts. As can be imagined, simulations that deal with millions of particles would suffer most if an inefficient contact detection algorithm is used. An example of an expensive algorithm would be to simply search for contacts by comparing each particle position against all particle positions in the simulation and then storing this contact information. Even for a small simulation of say, $n = 9$ particles, this would be $n(n-1) = 72$ particle-particle distance calculations. If a simulation has rapidly moving particles, it would require frequent contact list updates, which would increase on the time consumed by contact detection alone. Storage of information would also increase significantly as the number of particles grows making contact detection computationally expensive. There would also be a duplication of information in this type of search method.

Munjiza and Andrews (1998) [53] provide three requirements that should consist a contact detection method as follows:

1. *Minimization of CPU requirements, i.e. total detection time T as total CPU time needed to detect all couples close to each other.*

2. *Minimization of total memory (RAM) requirements M expressed in terms of total memory size as a function of total number of bodies and packing density.*

3. *Flexibility in terms of rate of M and T change with change in packing density.*

Before the contact search is initiated in any contact search algorithm, there needs to be some way to represent particles or objects. This can be done by simply drawing out the particle extents as the exact size and shape of the particle. This approach might be fine for a system containing few particles that

have regular shapes. As the number of particles increases, however, contact detection with this kind of representation would become slow. An alternative approach typically used is to construct a bounding box around each particle such that the entire particle is enclosed in this box as in Figure 2.7(a). For irregular shaped particles like those in [54], this would simplify the particle geometry during contact detection. Searches for contacts are initially done based on these boxes. A fine search is then done once bounding boxes are declared to be in contact. To ensure that contacts are detected early enough, a buffer zone can be added such that the box goes beyond the particle extent as in Figure 2.7(b) (see for example, [55]).

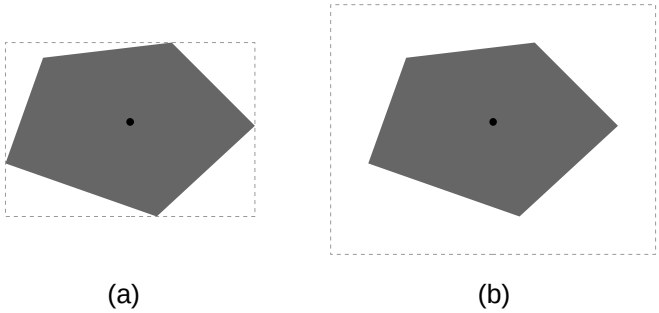

Figure 2.7: Body representation: (a) bounding box around particle with no buffer; (b) bounding box around particle with buffer.

Generally, contact search algorithms can be grouped into either binning-based schemes (also known as grid-based or cell-based approaches), or tree-based schemes. O'Sullivan [1] observed that binning-based schemes are relatively easy to implement and are most commonly used in DEM simulations. A binning-based approach was used in the simulations in this thesis that are described in Chapters 3. Binning-based schemes are, therefore, further explained below. Tree-based algorithms place the bounding boxes of each particle into a tree structure such that particles are divided into a parent and child relationships to define the tree connections. There are different criteria for specifying these relationships based on the method used. Han et al. [56] provide a good description of the approaches used in tree-based algorithms. [57–59] provide some examples of tree-based algorithms, that might be of interest to the reader. Han et al. [56] did a performance comparison between binning-based and tree-based schemes for regular shaped domains. They found that the binning-based schemes were more efficient for large particle systems with millions of particles with simulation speeds 40 times faster.

In the binning-based approach, a regular grid system is used to describe the problem domain such that each grid cell is typically large enough to contain the largest particle in the system. Each particle position coordinate would then be mapped on to a particular cell. Particle neighbours can then be established by inspecting the adjacent cells. Each particle would have a particle identification number (id) that would help track it during the simulation. Within the grid, each particle id would be associated to a row, column, layer, and cell numbers. When a particle(s) move(s) from outside of the current grid system, the grid system is redrawn and all the particles are remapped. To avoid constantly re-mapping, it is possible to specify a very large domain size to accommodate all the particle movements throughout the simulation time. This approach was adopted in version 5 implementation of the DEM Particle Flow Code (PFC) [55].

Contact searching happens in two stages: a course search and a fine search. In the course search, contact search compares each grid/cell against adjacent grids. Once contacting grids have been identified, particles within these grids are then checked for contact by comparing the distances between the bounding boxes surrounding each box. This provides the potential contacts. A fine search will then be done

on these potentially contacting particles to identify contacts. Care must be taken to avoid duplicating contact information. Examples of binning-based algorithms can be found in [55, 56].

2.1.3 Choosing a suitable time step

One of the challenges in contact detection is fast moving particles. To ensure that contacts are detected, a suitable time step needs to be used. Another reason, as has already been mentioned, is that particle accelerations need to be accurately calculated to avoid large movements at each time step. Guidance on how best to choose a time step for DEM studies like those presented in the next section has been provided by, for example, O'Sullivan and Bray [60]. In this thesis, the DEM critical time step proposed by O'Sullivan and Bray [60] for different particle arrangements, where the critical time step is given as $0.221\sqrt{m/K}$, where m is the mass of the smallest particle and K is the contact stiffness taken to be the greater of either the normal (K_n) or tangential (K_t) contact stiffness values: $K_n = 4G/(3(1-\nu))$, $K_t = 4G/(2-\nu)$, and $G = E/(2(1+\nu))$.

2.2 Applications of the DEM

Particulate systems in nature and industry have been studies using the DEM since the original work of Cundall and Strack [6]. There is an exponential growth in the number of papers associated with DEM [61, 62]. DEM simulations are done in both 2D and 3D. Since 2007 the number of studies that use 3D DEM has exceeded those done using 2D DEM simulations [62], which has been facilitated by HPC facilities in recent years. This section aims to provide a review of the application of this tool with a later focus on energy dissipation.

Before some of the studies on energy dissipation are reviewed, it is important to briefly discuss the use of the DEM generally. It is also important to acknowledge that there is a growing body of literature that has focussed on the development of DEM as a method. Some of these studies have been mentioned in the previous sections.

2.2.1 General applications of the DEM

Zhu et al. (2008) [63] did a review of the major applications of the DEM and provided the findings from these studies. They categorised the studies into three subject areas: particle packing, particle flow, and particle-fluid flow. These areas will be maintained for the purpose of the below general discussion of the applications of this method.

Particle packing can refer to either a settled state of a particle system or to the process by which this state is achieved. The process by which particles are packed will influence the material properties and characteristics. Understanding these processes can, therefore, be useful in industrial process that involve packing of granular material. This knowledge can also help in understanding more about collections of particles in nature such as soils.

In order to understand the structure of a packing, properties such as coordination number (CN), radial distribution function (RDF), and packing density or porosity are typically used. Both CN and RDF are micro (grain-scale) properties while packing density or porosity is a macroscopic property. The contact force network of a packing can also be used to describe a packing.

Packing density or porosity can be influenced by the method of packing used. Some of the particle generation methods in Section 2.1.1 can be viewed as packing methods. Zhang et al. (2001) [4] made some observations on the effect of dynamic variables on the packing of spheres. When a large amount of initial energy is used during packing by increasing the drop height, a dense pack is achieved (Figure

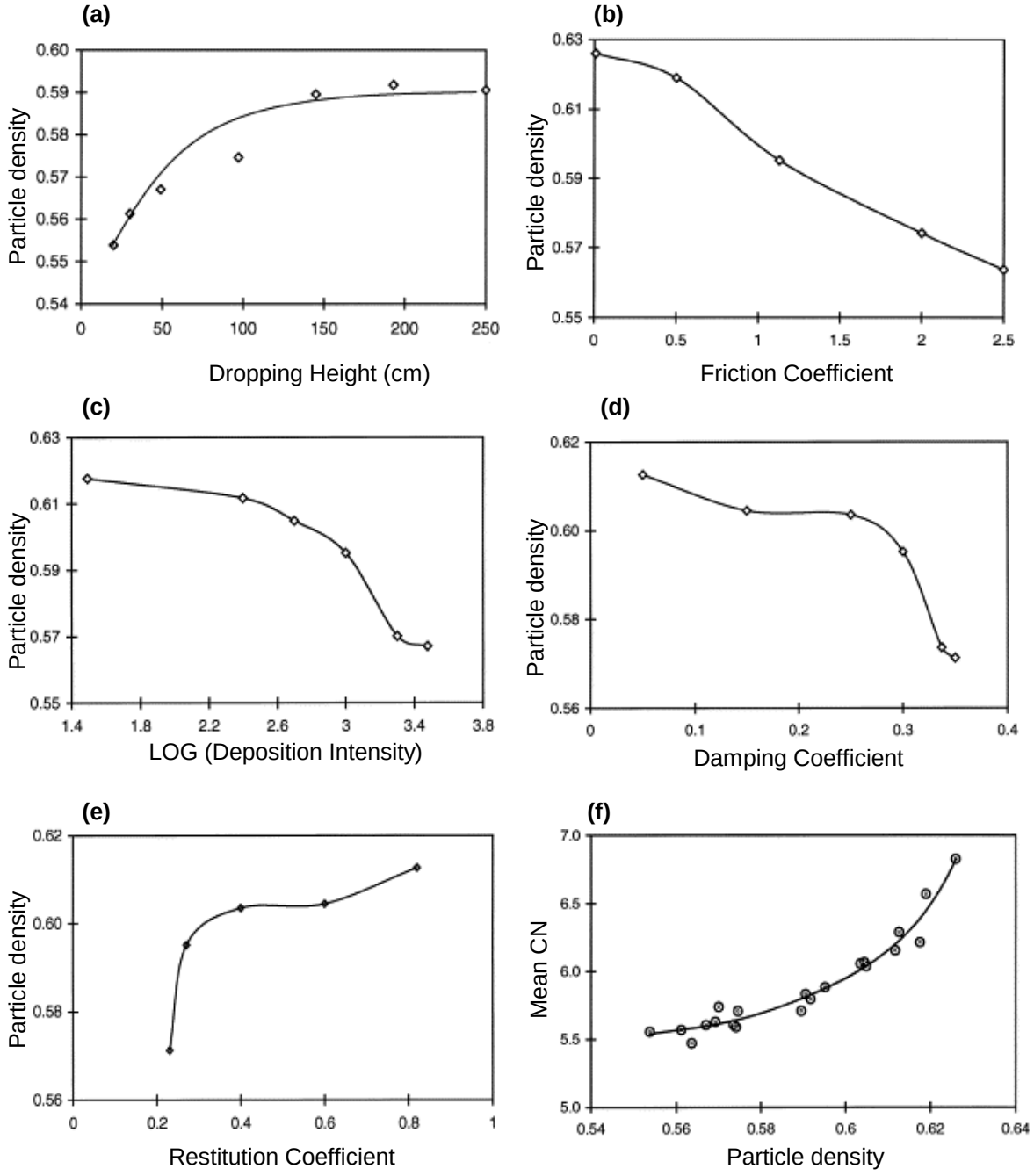

Figure 2.8: Results by Zhang et al. (2001) [4] using mono-sized spheres: plotting packing density as a function of (a) Dropping Height, (b) Friction coefficient, (c) deposition intensity, (d) damping coefficient, and (e) resititution coefficient. Results in (f) plot mean CN as a function of friction coefficient.

2.8(a)). This can be explained by noting that the high force required to push the particles together is achieved with increasing drop height. They also observed that an increase in the inter-particle coefficient of friction would lead to a looser sample packing (Figure 2.8(b)). A high deposition intensity was also associated with loose samples (Figure 2.8(c)). These observations were also seen in the work of Tangri et al. (2017) [64] who studied the packings of cylindrical particles with varying particle diameters.

Zhang et al.'s (2001) [4] mono-sized spheres when the damping coefficient is varied during particle

packing (Figure 2.8(d)) show a decrease in damping coefficient led results in a lower particle density. Also a decrease in the coefficient of restitution results in an a looser sample as observed in Figure 2.8(e).

Particle density has the potential to change the number of contacts per particle. This information can be captured by the CN, which is the number of contacts that each particle has. Often the average CN is taken for an entire particle system under study at given time points in the simulation. It can be expected that as the density increases, the average CN will also increase. This was observed in DEM studies Figure 2.8(f) for mono-sized spheres.

There are differences in the dominant forces of a particle packing depending on particle mass. Typically, systems with large particles of diameters greater than $\approx$100 μm will have particle inertia more dominant than the cohesive forces such that these surface attraction forces can be ignored. Sands for example are modelled in the DEM without the inclusion of any surface forces. Such particle material would be considered as non-cohesive or cohesionless. The simulations done in this thesis are on particle systems of this nature.

Cohesive forces are the kind that would cause a tendency of particles lumping together. Examples of such forces are van der Waals and electrostatic forces. These can be associated with fine particles such as clay particles. These forces will affect the nature of a packing significantly in particle systems that are described as cohesive. There are not so many DEM simulations done on such particle systems in comparison to the cohesionless systems partly due to the need for a large number of particles to realistically model fine particles, and the complexity involved in modelling cohesive forces. Examples of studies that include cohesion can be found in Zhu et al.'s review [63].

Compaction of particles is another interesting subject of study in particle packing as can be seen from the compaction studies by Martin and his colleagues [65–68]. Different mechanisms are involved during compaction such as particle rearrangement, plastic deformation, and particle breakage. In low pressure compaction, densification is achieved mainly through particle rearrangement, while plastic deformation is dominant in high pressure compaction. If particle breakage is considered, densification will involve the rearrangement of particle fragments. Studies have been done on particle crushing, for examples, [69, 70] Particle shapes, roughness, and sizes will determine how easily particles can be rearranged. The size of each plastic deformation, on the other hand, is influenced by the material properties.

Particle flow studies are concerned with understanding the behaviour of particle systems in motion. Most of the studies done in geomechanics fall within this area. O'Sullivan [62] presented a review of geomechanics studies using DEM and provided some of the distinguishing response characteristics of granular materials that have been successfully captured in DEM simulations. Some of the characteristics studied are: peak shear stress [71, 72]; hysteresis [73, 74]; the significance of the intermediate principal stress [75, 76]; strain softening [34, 77]; anisotropy of strength and stiffness [78, 79]; creep behaviour of soils and pore characteristics [80].

There have been several studies that have aimed at simulating laboratory experiments. This is because laboratory experiments can be more expensive than computational simulations. Another reason for this move is because microscopic characteristics of a material are more easily understood in a computational framework. Studies relating to one-dimensional compression and different shearing tests have aided in understanding particle flows. One-dimension tests would generally fall under particle packing while shearing tests are in the present category. Some of the shearing tests include:

- direct shear test, which is commonly used to measure the bulk strength of materials (example references; [81–86])
- biaxial compression, which has two directional stresses applied to a sample (example references;

[87–91])

- triaxial compression, which involves an application of a constant hydrostatic pressure to a specimen while imposing an axial stress from the top and/or bottom of the sample (example references [35, 36, 69, 92–96])
- annular (or torsion) shear, which involves twisting of the sample and is used for measuring the shear strength of soil (example references; [97, 98]).

Another kind of flow type is slow vertical flow. It is commonly encountered in industrial processes such as silos and hoppers. Studies in this area can help in understanding of quasi-static granular flows and have the potential of influencing industrial designs. Examples of DEM studies for this kind of flow can be founds in references [3, 99, 100].

The above mentioned particle flow studies would be classed are confined. Some examples of unconfined flow DEM studies include: landslides (e.g. [101]); excavations (e.g. [102]); earthquake damage (e.g. [103]). More examples of DEM particle flow studies refer to [63].

Particle-fluid flow studies include fluid interactions with particles. This type of coupling can be observed in almost all particle systems. To model this interaction, researchers typically couple DEM with Computational Fluid Dynamics (CFD). Zhao and Shan [104] provided some good examples of geomechanics applications of CFD-DEM. More general particle-fluid flow DEM studies can be found in ref. [63].

Before transitioning to energy dissipation, it is worth touching on DEM result validations. These are currently done by comparing with existing experimental data where available. For example Cundall and Strack [6] validated the DEM model by replicating the experiments on steel spheres described by Rowe [105]. O'Donovan [106] used this same process. Comparing of standard laboratory tests and simulation results is another way of validating results. For example, O'Sullivan and Bray [60] used biaxial compression test results. Other validation methods are provided in a dedicated paper by O'Sullivan et al. [72].

2.2.2 Energy dissipation in geomechanics

Energy monitoring is important to the study of dissipation in granular media. Little exists in the literature explaining how this is done despite its increasing interest in DEM simulations. To account for the dissipated energy, energy conservation is applied. Houlsby et al. [107] for example, in the study of landslides took the dissipated energy to be the remainder of the total potential energy at the start of the simulation minus the sum of the potential energy and the kinetic energy at each stage of the simulation. Asmar et al. [108] explicitly worked out the dissipated energy from damping and friction, the main contributors to energy dissipation as discussed below. Other forms of energy: the elastic energy stored in the contacts, potential energy, kinetic energy, and the input energy were also monitored. Wang and Yan [109] were explicit in their energy calculations and included bond energy for their simulations since they considered particle crushing. Another example of explicit energy calculations is the work of Hanley et al. [96], however, this study did not include particle crushing since it has been shown to account for very little energy in comparison to other energy terms (see for example [109–111]).

Wang and Yan [109] showed that at every stage of shearing (in the direct shear test of agglomerates), the conservation of energy equation is given by

$$\Delta W + \Delta W_g = \Delta E_s + \Delta E_b + \Delta E_f + \Delta E_k + \Delta E_d, \tag{2.13}$$

where the energy terms are: boundary work ΔW, potential energy ΔW_g, strain energy ΔE_s, bond energy ΔE_b, frictional dissipation ΔE_f, kinetic energy ΔE_k, and damping dissipation ΔE_d. This equation provides a general energy balance form, which is consistent with other literature (for example, [108, 112]) with the effects of particle bonding ignored if negligible or if not considered. The energy loss due to dumping can either arise as a result of accounting dissipating excess kinetic energy in the system.

There have been a number of papers in recent years that have discussed energy dissipation. Zhang et al. [113] investigated the relationship between energy dissipation and shear band formation under rolling resistance. The effect of grain roughness on energy dissipation was investigated during a quasi-static homogeneous triaxial compression test on cohesionless sand under constant lateral pressure [114]. A dissipation consistent fabric tensor definition was provided by Li and Dafalias [115] from their DEM simulations. Shamy and Denissen [116] studied energy dissipation response due to seismic loading by monitoring the energy on a microscopic level. Daudon et al. [117] showed that particle shape and slope geometry where the major factors leading to energy dissipation in a rock avalanche.Energy balance and dissipation were studied in a DEM based study of the standard penetration test by Zhang et al. [112]. These are some of the examples of the many studies done on energy dissipation in geomechanics.

DEM has been instrumental in the study of incremental response of soils. It is possible to use laboratory experiments but there are difficulties involved hence the use of DEM [118]. Calvetti et al. [119], for example, studied the incremental behaviour of soils by carrying out a series of stress probes of varying directions and found that a classical plasticity with a single plastic mechanism is able to describe the behaviour. Understanding of these responses can help in the studies of energy dissipation.

Energy monitoring is important in the development of continuum constitutive models. O'Sullivan [1], for example, by referencing [120] reports that the Cam Clay yield locus, which is determined by integration of the flow rule, is determined from the work of plastic deformation. Comparisons between DEM energy dissipation results to constitutive models have sometimes been done. Bolton et al. [121] compared their energy dissipation results of crushable particles to both Cam Clay and modified Cam Clay dissipation function. Hanley et al. [96] also compared their results from non-crushable particles with modified Cam Clay functions and recommend improvements to the modified Cam Clay model, which they believe ensure more accurate modelling based on their observations. These studies highlight the importance of understanding energy dissipation in granular media so that continuum constitutive models can be developed more accurately. The current thesis adds to this body of work by studying the influence of particle size distribution, void ratio, and inter-particle friction coefficient on energy dissipation in one-dimension compression tests.

Parameters and characteristic that influence dissipation

In studies of energy dissipation, there is a growing interest to understand those key parameters that influence energy dissipation in granular media. This knowledge can facilitate a more accurate development of constitutive models. Grain roughness, confining pressure, particle size distribution, displacement rate, damping factors, cohesion, and viscosity are some of the parameters shown to influence energy dissipation.

Wang and Arson [111] did a study of energy distribution in a quasi-static confined particle system on crushable particles by running uniaxial compression tests. From their study, they observed that at least 60% of energy was lost through friction as a result of particle rearrangement. The rest of the energy was either lost through particle breakage (less than 5%) or stored within contacts. This study did show that friction is indeed the biggest contributor to energy dissipation. Other authors have also noted that friction is the main cause of energy dissipation in soils (e.g. [107, 109, 122]).

Cohesion has also been shown to be directly related to energy dissipation (e.g. [123]). A number of

authors have studied cohesive soils but not focussed so much on the energy dissipation (e.g. [124, 125]). Moreno-Atanasio [126] showed that the breaking of particle cohesive forces when particles hit a rigid target was energy dissipative. The study highlighted, however, that this was less than 10% of the total energy dissipated.

The confining stress level was also shown as an indirect, nonetheless important, contributor to energy dissipation in soils, particularly for crushable materials ([127]). There is a strong dependence of particle crushing on the confining stress level. High confining stress levels however lead to significant peak shear stress ratio reductions and considerable volumetric compression due to increased particle crushing.

Zhang et al. [113] did a comprehensive study on the energy dissipation due to inter-particle rolling resistance. The simulation results indicated that inter-particle sliding and rolling are particle mechanisms that work together to dissipate a minimum amount of energy and advance the material fabric evolution. Since rolling resistance (or rolling friction) is as a result of particle roughness and shape irregularity, it can be incorporated in DEM as a shape parameter to account for these surface irregularities (e.g. [128]).

Damping is another cause of dissipation in DEM simulations [129]. This has been discussed in various forms by some authors (e.g [121, 130]). A higher damping ratio leads to more energy dissipation as expected.

Another not so well studied parameter in relation to energy dissipation that needs further investigation is the particle size distribution (PSD). Though not studying soils or using DEM, Lin and Hwang [131] showed that samples with narrower PSDs had more heat dissipation than those with wide distributions. Their focus was heat dissipation of heat-pipes with sintered porous wicks, which used gas-atomized cupper powders of different PSDs. Clearly linked to PSD is the voids ratio. The lower the voids ratio, the more energy dissipated. This was observed from the result of Kozicki et al. [132] when they did DEM simulations of a triaxial compression test for sand.

Soil water content is another parameter worth investigating in relation to energy dissipation. A CFD-DEM coupling would potentially help investigate this further. Though not using DEM, McNamara [133] did a study on energy dissipation in relation to soil-moisture hysteresis and found that energy is dissipated through heat during a water content change.

There is certainly more parameters that need to be discovered that influence energy dissipation. But it appears to be the case that any parameter that would influence friction or damping would contribute to most energy dissipation in granular media.

2.2.3 Conclusions on applications

Although the DEM started as a geomechanics tool, it has gained so much popularity in many fields of research. This has mainly been facilitated by the significant improvements in computing power in the past decades.

The ability of DEMs to capture physically hard to measure parameters has aided the study of those parameters that influence energy dissipation in Chapter 3. The simulations in Chapter 3 were carried out using a 3D code described in the next section. There are several DEM codes used in research, some of which are mentioned in the next section.

2.3 LIGGGHTS

As mentioned in Chapter 1, LIGGGHTS [24] was used for the other simulations that will be presented in this thesis.

2.3.1 LIGGGHTS scripting

In LIGGGHTS, the user drives a simulation using a text-based input script containing a series of commands to conduct the simulation. This input script is read sequentially rendering the ordering of the statements important. A typical script will consist of four parts:

1. *Initialization:* The parameters that need to be defined before the particles are created are set. Such parameters can include the type of boundary to be used, the type of units to work with (typically SI units), the domain to run the simulation in, type of particles, among others.

2. *Setup:* Here the material properties are defined as well as the geometry. The particle generation procedure is also detailed.

3. *Detailed settings:* Define settings that correspond to speed and memory utilisation. Include output options and any other necessary settings for the problem.

4. *Execution:* This is the actual run command that executes the simulation.

Almost all problems will have multiple execution steps within one simulation. In such cases, the problem is split into smaller problems within the script using different statements. There are two basic types of statements in a LIGGGHTS input deck - individual commands and fixes. The commands establish the settings of the simulations (e.g. the time step) while the fixes are used to set particular aspects of the simulation (e.g. material properties and boundary conditions).

Some boundary geometries can be defined within the input script using a fix statement. These, however, will not be visible at the end of the simulation during post processing. If the user wants to visualise a geometry, they would need to create a separate mesh, for example in a CAD software, and input it as a STereoLithography (STL) file via a fix statement in the input script.

Once the simulation is complete, the output files can be run through the LIGGGHTS Post-Processing (LPP) software in which the Visualisation Toolkit (VTK) files will be generated. These can then be visualised in any software that can open VTK files (e.g. ParaView [134]). Post processing of the results can then be readily done. If required during post processing, a log file updated throughout the simulation can also be referred to.

The simulations done in Chapter 3 are one-dimensional compression tests. Examples of how the scripts for these simulations look like will be provided as will be discussed in those chapters. Some of the challenges that were encountered while using LIGGGHTS are discussed next

2.3.2 Challenges using LIGGGHTS

Neighbour list problems. It was found that the ratio between the largest particle and the smallest particle should not be significantly large in the version of LIGGGHTS used (version 3.6). When this was done, the particle simulations either took very long to run or failed due to neighbour list error messages.

Particle size distribution set ups. It was found that the particle size distributions desired were not always obtained. To overcome this, particles were inserted at lower sizes and then grew to the full size. Another method to overcome this challenge would be inserting particles at zero friction coefficient and then change the friction coefficient later in the simulation.

Running simulations in parallel. At first glance it might seem obvious that the more processors used to run a simulation would result in a shorter runtime. But this is not necessarily the case. The time spent on communication between processors could potentially slow down the simulation significantly. LIGGGHTS users recommend that each processor should have a few hundreds of particles on it. The

simulation grid size is distributed in the x y and z directions. If the simulation sample is of cubic shape, then an equal number of processors would be required in all directions. To work this out, one would need to divide the total number of particles by a minimum of 100 then do the cube root to get the number of processors required in each direction. The speed up is also dependant on how many particles from one processor interact with those in other processors, and on the various sizes of particles.

Limitations on outputs. In earlier versions of LIGGGHTS, some of the contact information needed for energy dissipation calculations was not provided as an output option. This was overcome by calculating the desired outputs in during post processing in Matlab. Another option that could have been employed is extending the LIGGGHTS code to include these outputs. This was, at the time, seen as a more time consuming process that was not necessary for the required simulations.

2.4 Observations

"The use of DEM to study soil micromechanics may inform development of more sophisticated and reliable continuum models, and thus have an indirect impact on engineering practice." O'Sullivan [1]

Those words sum up the motivation behind using DEM in this thesis. This chapter has shown that the DEM is a reliable tool for studying granular media. It is able to capture physically difficult to measure granular behaviour making it an attractive tool to study energy dissipation in granular media. The next chapter will explore energy dissipation in one-dimensional compression tests through a parametric study.

Chapter 3

One-dimensional compression

3.1 Introduction

Chapter 2 showed that DEM is a reliable tool for studying granular media. In this present chapter, the DEM will be used to study energy dissipation in one-dimensional compression tests.

Energy dissipation in granular media has been a subject of study in recent years using the DEM. Wang and Huang [135], for example, presented a DEM analysis of energy dissipation in crushable soils where it was observed that crushability affects energy dissipation by creating more contacts as particle break leading to more energy dissipation through friction. Zhang et al. [113] investigated the relationship between energy dissipation and shear band formation under the rolling resistance caused by irregular particle shapes and surface roughness. The effect of grain roughness on energy dissipation was investigated during a quasi-static homogeneous triaxial compression test on cohesionless sand under constant lateral pressure in [114, 116].

However, the focus of this chapter is on obtaining a link between energy dissipation and the grain scale parameters of granular media under one-dimensional compression. Even though computational power has improved significantly over the years, it is still not possible to do large-scale analysis using DEM. It is, therefore, envisioned that the findings in this chapter can help inform the formation of continuum function linking energy dissipation to grain scale parameters.

The rest of this chapter is organised as follows: Section 3.2 will provide the simulation procedure followed, Section 3.3 will discuss the parameters studied, Section 3.4 will explain the process followed in evaluating the energy dissipated post the simulations, Section 3.5 will discuss the results from the simulations, and conclusions will be drawn in Section 3.6.

3.2 Simulations procedure

An open source DEM particle simulation software, LIGGGHTS, developed by Kloss et al. [25] was used to model one-dimensional compression of samples of spherical particles. Each sample was 18mm in diameter and 10mm high bound by a STereoLithography (STL) mesh with zero friction between the particle to mesh interface. Each simulation had a densification stage to reach the target void ratio before the loading and unloading cycles. The script of each simulation followed a similar format, the lines of which are discussed next.

A set of thirteen variables were set at the beginning of each of the simulation scripts as shown in Algorithm 3.1. The syntax of variable is variable *name style args*, where the *name* is case sensitive and is used to initiate the variable during calls in the script, *style* includes several options that assign values to the variable (for example, *equal*), and *args* are the quantities assigned to the variable, which can be

characters, numbers, or even formulas to be evaluated. The thirteen variables in Algorithm 3.1 that were specified have each an explanation provided as # comments where # comments are not executed during

Algorithm 3.1 Initial simulation variables

```
1  variable dt equal 0.0000001          #Time step
2  variable ins_steps equal 500000      #Time steps for insertion
3  variable set_steps equal 1000000     #Time steps for settling
4  variable tlim equal 5000000          #Maximum time steps per cycle
5  variable every equal 25000           #Time step interval for outputs
6  variable R equal 0.009               #Radius of simulation extent
7  variable H equal 0.01                #Height of simulation extent
8  variable rho equal 2650              #Density of each particle
9  variable const equal PI*(${R})^2     #Constant for later volume calculations
10 variable v_dens equal 0.000000025    #Speed to densify at in m/s
11 variable v_comp equal 0.000003       #Speed to compress at in m/s
12 variable vra_dens equal 0.7          #Target void ratio during densification
13 variable vra_comp equal 0.2          #Target void ratio during compression.
```

the simulation. To ensure a stable simulation, a time step, Δt of 1×10^{-7}s was used (which is dt in line 1 in Algorithm 3.1 above). This value was arrived at based on the method for calculating the DEM critical time step proposed by O'Sullivan and Bray [60] for different particle arrangements, where the critical time step is given as $0.221\sqrt{m/K}$, where m is the mass of the smallest particle and K is the contact stiffness taken to be the greater of either the normal (K_n) or tangential (K_t) contact stiffness values: $K_n = 4G/(3(1-\nu))$, $K_t = 4G/(2-\nu)$, and $G = E/(2(1+\nu))$. For a stable simulation, a value equal to or less than the critical value needs to be used. To ensure that the simulation did take several days to run, the number of time steps was set to certain limits. In Algorithm 3.1: the time steps to insert particles was set in line 2; the settling time steps to allow particles to settle was set in line 3 by taking guidance from example LIGGGHTS simulations in the documentation [24]; each simulation cycle was limited to the time steps in line 4; and the interval time steps to limit how often files were output was set in line 5. Lines 6 through to 13 are as explained above. The value in line 8 will be explained below together with the properties of each particle. Line 12 had initial void ratios, e_{ini} values in the range [0.7 0.43] for different simulations.

Essential settings for each simulation before the particle insertion stage were set as in Algorithm 3.2. In line 15 the particles were set to granular style, which meant that the effects of particle forces did not

Algorithm 3.2 Essential simulation settings

```
14 echo both                          #Each command is echoed on the screen and log file
15 atom_style granular                #Particles would be associated with granular models
16 atom_modify map array              #Particles IDs are stored in array lookup
17 communicate single vel yes         #Single distance communication and store velocities
18 boundary f f m                     #Fix boundaries except in the z-direction
19 newton off                         #Set bonded interactions off
20 units si                           #Assume international system of units
21 region  reg cylinder z ${R} ${R} ${R} 0.0 ${H} units box #Define region 'reg'
22 create_box 1 reg                   #Create simulation container defined by region 'reg'
23 neighbor 0.001 bin                 #Typical neighbour cut off distance when using SI units
24 neigh_modify delay 0               #No time delay when calculating particle neighbours
25 shell rm -rf post                  #Remove post folder if it exists
26 shell mkdir post                   #Create post forlder to store files during the simulation
```

go beyond the immediate neighbours. Atom information was set to be mapped in arrays according to line 16, which meant the particle ID lookup was done from an array store. Line 17 enabled each processor to obtain information of particle information within a single distance from its sub-domain. In line 18 boundaries were set to be fixed in the x and y axes, but moving in z-axis, which meant that the boundary

dimensions could only change in the z direction. Line 19 ensured that no bonding effects are calculated. The simulation region was described line 21 as a cylinder with radius set to the value in variable R from line 6 about the z axis with x and y coordinates also set using variable R. The height was set from a low of zero to H. Both R and H were provided in Algorithm 3.1. The simulation region was then created in line 22 where the value 1 meant that there was only one particle type in the simulation. In line 23 particle neighbours were set to be detected using the bin scheme as described in Chapter 2 with a buffer distance around each particle set to 0.001m. The buffer value here is the typically used value in LIGGGHTS simulations [24] when SI units are used. The current author also found it to work best for all simulations conducted since lower values resulted in particles escaping the bounding region. Particle contacts were set to be detected at every time step according to line 24. Lines 25 and 26 were used to create a folder to which files were to be written for post processing.

The material properties of each particle were set as shown in Algorithm 3.3. As shown in lines 28

Algorithm 3.3 Material properties

```
28  fix    m1 all property/global youngsModulus peratomtype 7.e10
29  fix    m2 all property/global poissonsRatio peratomtype 0.25
30  fix    m3 all property/global coefficientRestitution peratomtypepair 1 0.3
31  fix    m4 all property/global coefficientFriction peratomtypepair 1 0.5
32  pair_style gran model hertz tangential history     #Hertzian without cohesion
33  pair_coeff  * *
```

and 29, the simulated particles were spheres each of Young's modulus, E of 70GPa and Poisson's ratio, ν of 0.25 for all particle groups, which are typical values used in the literature (e.g. [19, 136, 137]). The coefficient of restitution value for particle type 1 was set to 0.3 in line 30, a value that was seen in the example simulations presented in LIGGGHTS documentation. The coefficient of friction between particles of type 1 was set in line 31 with values for different simulations $\in$ [0.25, 0.5]. The particle contact model was set to Hertz-Mindlin in line 32.

In Algorithm 3.4 the time step and gravitation force were set where dt is defined in Algorithm 3.1 and

Algorithm 3.4 Time step and gravity specification

```
34    timestep ${dt}                                  #Set the time step that value
35    fix gravi all gravity 9.81 vector 0.0 0.0 -1.0  #Gravity act in negative z-direction
```

the gravity acts in the negative z-direction.

Wall boundaries were inserted as meshes in lines 36-38 in Algorithm 3.5. where the walls were set to

Algorithm 3.5 Wall boundaries

```
36    fix stressmesh all mesh/surface/stress file meshes/SmallSample3.stl type 1 stress on
37    fix stresslidmesh all mesh/surface/stress file meshes/SmallSamplelid3.stl type 1
          stress on
38    fix granwalls all wall/gran model hertz tangential history mesh n_meshes 2 meshes
          stressmesh stresslidmesh
```

be of particle type 1 so that they act as particles in order for other particles to "see" the walls, and stress calculations on each mesh were allowed according to lines 36 and 37 for later storage. Line 38 then set formed the bounding walls from the mesh identifications tags, *stressmesh* and *stresslidmesh*. Line 38 also set the contact model for the wall as that for the particle-particle contacts.

Particle size distribution (PSD) to be used during the particle insertion stage was then stated, for example, as in Algorithm 3.6 where different simulations had different PSDs. Lines 39-45 describe different

Algorithm 3.6 Particle size distribution specification

```
39  fix pts1 all particletemplate/sphere 1 atom_type 1 density constant 2650 radius
        constant 0.0009
40  fix pts2 all particletemplate/sphere 1 atom_type 1 density constant 2650 radius
        constant 0.0008
41  fix pts3 all particletemplate/sphere 1 atom_type 1 density constant 2650 radius
        constant 0.0006
42  fix pts4 all particletemplate/sphere 1 atom_type 1 density constant 2650 radius
        constant 0.0004
43  fix pts5 all particletemplate/sphere 1 atom_type 1 density constant 2650 radius
        constant 0.0003
44  fix pts6 all particletemplate/sphere 1 atom_type 1 density constant 2650 radius
        constant 0.0002
45  fix pts7 all particletemplate/sphere 1 atom_type 1 density constant 2650 radius
        constant 0.0001
46  fix pdd1 all particledistribution/discrete 123457 7 pts1 0.053 pts2 0.12 pts3 0.28
        pts4 0.21 pts5 0.24 pts6 0.085 pts7 0.012
47  group   nve_group region reg
48  fix   ins nve_group insert/pack seed 1000003 distributiontemplate pdd1 insert_every
        10000 overlapcheck yes all_in yes vel constant 0.0 0.0 -15 region reg
        particles_in_region 16000
```

spherical particles that were used. Each particle had a density of 2650kg/m^3, which is a typical value used in slice sand (e.g. [19, 137]). Line 46 describes how the particle sizes were to be distributed during the random particle generation and insertion stage of the simulation in such a way that the sum of all weight contributions from each particle template from lines 39-45 is equal to 1. In line 46 the number 123457 is a seed number unique to this command used by LIGGGHTS to track it, and 7 is the number of particle templates used corresponding to lines 39-45. Line 47 was a necessary group created to be used for particle insertion in line 48. The particle generation and insertion method was done based on the description in line 48 such that random particles were generated every 10,000 time steps with a velocity of 15m/s downwards. This high velocity was set to allow particles to settle quickly and free up more space required to randomly generate other particles. LIGGGHTS does not always yield the desired PSD during the particle generation stage. This is dependant on the particle insertion method used and the number of time steps run at the particle generation stage. The author generated samples with PSDs of coefficient of uniformity, C_u values of $\in [1, 2]$. The coefficient of uniformity is a shape parameter that can be used to measure PSDs. It is calculated as

$$C_u = \frac{d_{60}}{d_{10}}. \tag{3.1}$$

d_{60} and d_{10} respectively are particle diameters for which 60% and 10% of the material by mass is finer.

Particle information at every time step was updated based on the command in Algorithm 3.7 so that

Algorithm 3.7 Particle information update

```
49  fix   integr all nve/sphere
```

the particle positions, velocities, and angular velocities were updated at every time step by treating the particles as finite size spheres rather than points.

Outputs on the screen were enabled using *thermo* commands where a customised output list of the current time step, the number of atoms, the kinetic energy, and the simulation volume were output according to line 50. Line 51 ensured that this information was output every 1000 time steps. Screen outputs help the user to have a quick look at the simulation progress. They, however, slow down the simulation when too frequent. Since the current number of particles in the simulation region were

Algorithm 3.8 Data output settings

```
50  thermo_style  custom step atoms ke vol
51  thermo    1000
52  thermo_modify lost ignore norm no
53  variable kner equal ke
```

to be output according to line 50, calculations for any particles that would go beyond the simulation region were prohibited in line 52. However, no particles were lost during the simulations reported in the present chapter since less calculations would have been done in such case. This was simply added for the simulations to terminate quicker if a such a problem arose. The variable *kner* in line 53 was set to store the kinetic energy to be output to a file as will be described below.

To make contact information accessible, *compute* commands for particle-particle and particle-wall contacts were included as in Algorithm 3.9. Line 54 was for particle-particle contacts: normal and

Algorithm 3.9 Contact information to be output

```
54  compute pairsP all pair/gran/local pos vel id force_normal force_tangential
        contactArea delta
55  compute pairsW all wall/gran/local pos vel id force_normal force_tangential
        contactArea delta
```

tangential contact forces, contact area, and particle overlap. Line 55 was for particle-wall contacts: normal and tangential contact forces, contact area, and particle-wall overlap.

To execute the commands in the input script, a *run* command is called. Run commands are executed by running all the commands before it. Any command that needs to be removed can be removed by using delete equivalents of that particular command type (for example, a *fix* command can be removed by using the *unfix* command). Run commands were, therefore, stated and executed first for particle generation as shown in Algorithm 3.10. Line 56 ensured that DEM calculations were done for up to

Algorithm 3.10 Particle generation

```
56  run ${ins_steps} upto
57  unfix ins
58  run ${set_steps}  #run to let particle settle.
```

ins_steps time steps. During this run period, all the settings described in the above lines were executed and particle generation was done. Line 57 ensured that the particle insertion stage would end at the next run command. Samples had different particle numbers at the end of the particle insertion stage here grouped based on the coefficient of uniformity, C_u value. A sample of $C_u = 1$ had 977 particles, for $C_u = 1.3$, 1154, and for $C_u = 2$, 1734. Line 58 allowed particles to settle. A top view of the these samples is given in Figure 3.1 where in each sample, different colours corresponded to a different particle size.

Before the loading cycle, the particles were densified to different initial void ratio values in the range $\in$ [0.43, 0.7] by moving the top platen downwards at constant velocity, following which the particles were allowed to settle. A range of initial void ratios used to study their influence on energy dissipation. The samples were densified and the particles allowed to rest as in Algorithm 3.11. Lines 59-68 describe a series of calculations that were done to derive the top mesh velocity, *v_dens* and the number of time steps, *tdense* that were used to increase the sample density. The mass of the particles was calculated in line 59 and used to calculate the volume of particles in line 60. Line 61 calculated the total volume allowing for the current void ratio to be calculated in line 62. The target sample height was then calculated in

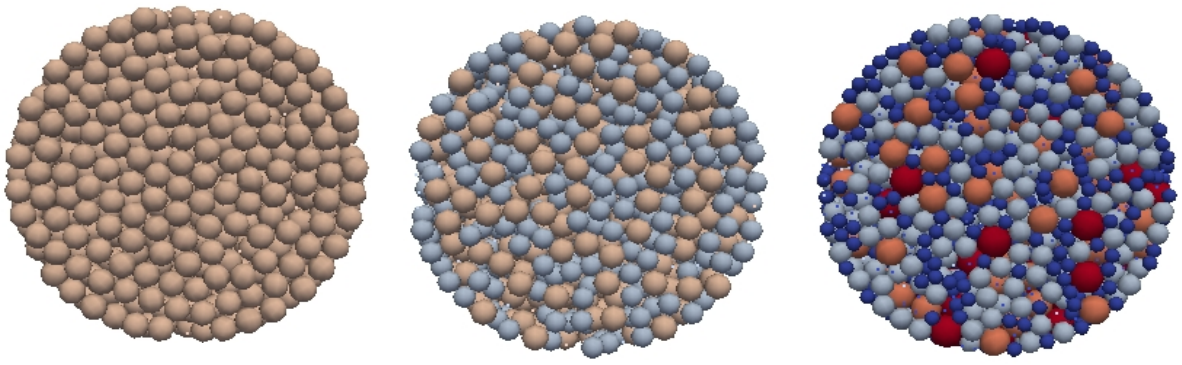

$C_u = 1$ $C_u = 1.3$ $C_u = 2$

Figure 3.1: Top view of particles according to their Cu values. The different colours are aids to visualise different particle sizes.

Algorithm 3.11 Sample compression to reach target density

```
59    variable mass equal mass(all)
60    variable vol_pcls equal ${mass}/${rho}
61    variable vol_box equal ${H}*${const}
62    variable void_ratio equal (${vol_box}-${vol_pcls})/${vol_pcls}
63    variable H_den equal ((1+${vra_dens})*${vol_pcls})/${const}
64    variable diffH_den equal ${H}-${H_den}
65    if "${diffH_den}>0.0" then "variable tdense equal round((${diffH_den}/${v_dens})/${dt
          })"
66    if "${diffH_den}<=0.0" then "variable tdense equal 1"
67    if "${tdense}>${tlim}" then  "variable v_dens equal ${diffH_den}/(${tlim}*${dt})"
68    if "${tdense}>${tlim}" then "variable tdense equal ${tlim}"
69    fix movecad all move/mesh mesh stresslidmesh linear 0.0 0.0 -${v_dens}
70    run ${tdense}
71    unfix movecad
72    run ${set_steps}  #run to let particle settle
```

line 63 and the difference between the current sample height and the target height determined in line 64. The information obtained thus far then allowed for the calculation of the required number of time steps, *tdense* and the top mesh velocity, *v_dens* in lines 65-68. A limit was set for *tdense* in line 68 to *tlim* obtained from Algorithm 3.1 because otherwise the simulation exceeded the 3 day time limit for simulations on the super computers the author used. The use of super computers allowed for many simulations to be run simultaneously as opposed to using the author's computer. It also allowed for the perfecting of the particle generation process by trying many samples. In line 69, the top mesh was set to move downwards at a downward velocity *v_dens*. This stage of the simulations was run for *tdense* time steps according to Line 70. In Line 71, the top mesh was stopped before the particles were allowed to settle by running for *set_steps* time steps in line 72.

Outputs to files for later post processing for the loading and unloading cycles were then set as in Algorithm 3.12. Line 73 output particle information and the simulation region coordinates to ASCII files. Line 74 output wall stress values to ASCII files. Line 75 and line 76 output particle-particle and particle-wall contact information respectively to ASCII files. Lastly, line 77 printed the kinetic energy values to a csv file. The values output in these files were later used in the energy dissipation evaluation stage described in Section 3.4 and to produce the results in Section 3.5.

After being densified, the particles were then compressed to a target void ratio, e_{tar} 0.2 on the loading cycle then unloaded for the same number of time steps used on the loading cycle. The top platen velocity

Algorithm 3.12 File output settings

```
73  dump    dmp all custom ${every} post/dump.1DCompression id type x y z ix iy iz vx vy
        vz fx fy fz omegax omegay omegaz radius
74  dump    dumpstress all mesh/gran/VTK ${every} post/dump*.vtk stress stressmesh
        stresslidmesh
75  dump    dmpPairP all local ${every} post/dump.1DPairsP c_pairsP[1] c_pairsP[2]
        c_pairsP[3] c_pairsP[4] c_pairsP[5] c_pairsP[6] c_pairsP[7] c_pairsP[8] c_pairsP
        [9] c_pairsP[10] c_pairsP[11] c_pairsP[12] c_pairsP[13] c_pairsP[14] c_pairsP[15]
         c_pairsP[16] c_pairsP[17] c_pairsP[18] c_pairsP[19] c_pairsP[20] c_pairsP[21]
        c_pairsP[22] c_pairsP[23]
76  dump    dmpPairW all local ${every} post/dump.1DPairsW c_pairsW[1] c_pairsW[2]
        c_pairsW[3] c_pairsW[4] c_pairsW[5] c_pairsW[6] c_pairsW[7] c_pairsW[8] c_pairsW
        [9] c_pairsW[10] c_pairsW[11] c_pairsW[12] c_pairsW[13] c_pairsW[14] c_pairsW[15]
         c_pairsW[16] c_pairsW[17] c_pairsW[18] c_pairsW[19] c_pairsW[20] c_pairsW[21]
        c_pairsW[22] c_pairsW[23]
77  fix energetics_try all print 2500 "${kner}" file energetics.csv screen no title "kin"
```

and the time steps required for these cycles were calculated according to Algorithm 3.13. The target

Algorithm 3.13 Mesh velocity calculation for compression testing

```
78  variable H_comp equal ((1+${vra_comp})*${vol_pcls})/${const}
79  variable diffH_comp equal ${H}-(${v_dens}*${tdense}*${dt})-${H_comp}
80  if "${diffH_comp}>0.0" then "variable tcomp equal round((${diffH_comp}/${v_comp})/${
        dt})"
81  if "${diffH_comp}<=0.0" then "variable tcomp equal 1"
82  if "${tcomp}>${tlim}" then "variable v_comp equal ${diffH_comp}/(${tlim}*${dt})"
83  if "${tcomp}>${tlim}" then "variable tcomp equal ${tlim}"
```

sample height was calculated in line 78 and the difference between this height and the current height calculated in line 79. The top platen velocity, *v_comp* and the required time steps, *tcomp* were then determined in lines 80-83. As in the desification simulation stage, *tcomp* was limited to *tlim* obtained in Algorithm 3.1. The loading and unloading cycles were then executed according to Algorithm 3.14 where

Algorithm 3.14 Compression testing steps

```
84  fix movecad1 all move/mesh mesh stresslidmesh linear 0.0 0.0 -${v_comp}
85  run ${tcomp}
86  fix movecad1 all move/mesh mesh stresslidmesh linear 0.0 0.0 ${v_comp}
87  run ${tcomp}
```

line 84 sets the top mesh to move downwards with velocity *v_comp* for time steps *tcomp* shown in line 85 before reversing the top mesh movement in line 86 for the same time steps in line 87.

Figure 3.2 shows an example of simulation before (a) and at the end of loading (b), and at the end of unloading (c). The next section will discuss the parameters varied for the simulations that were carried out within this chapter.

3.3 Simulation parameters

This study is focussed on the influence of two grain scale parameters coefficient of uniformity and inter-particle coefficient of friction, and the response to initial void ratio on the energy dissipation under 1D compression.

The coefficient of uniformity, C_u calculated using Equation (3.1), is a measure of soil gradation commonly used in civil engineering laboratories. Values greater then 4 show that the soil is well graded because it has a wide range of particle sizes. Values less than 2 show that the soil is poorly graded, for example beach sands. Grading can affect the critical states as studied by Muir Wood and Maeda [138].

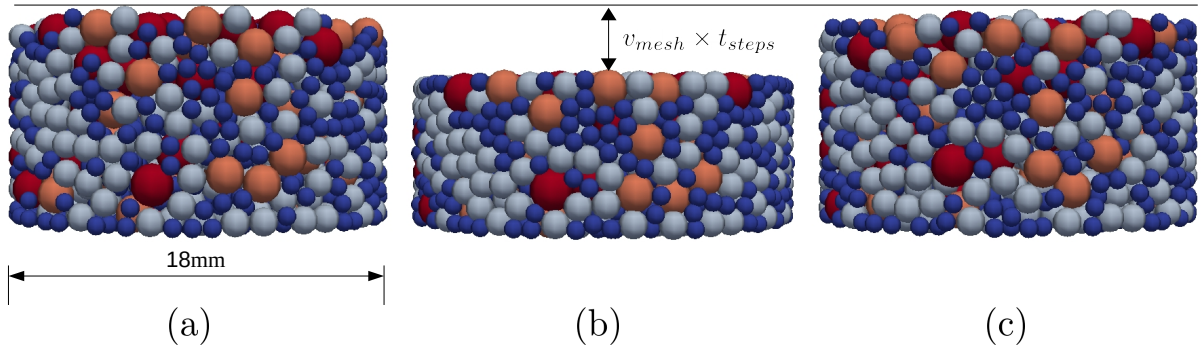

Figure 3.2: Loading and unloading: (a) before loading samples; (b) end of loading; (c) end of unloading.

Although their DEM simulations were on two-dimensional assemblies, they found that changes to grading lead granular material to seek new critical state conditions.

Friction between particles, μ is a major contributor to energy dissipation in granular media. The friction coefficient between particles was therefore varied along with the PSD and the initial void ratio, e_{ini}. Table 3.1 shows the values of the varied parameters for each simulation. The range of values were chosen to supply a good range of values except for the C_u values, which were a consequence of the simulation particle generation procedure as explained in Section 3.2. Results from these simulations are discussed in Section 3.5. But first, the post processing of the DEM results for energy dissipation is presented.

Table 3.1: 1D Compression Simulation test parameters

C_u	e_{ini}	μ
$\in$ [1, 2]	0.7	0.5
2	0.7	$\in$ [0.2, 0.5]
2	$\in$ [0.43, 0.7]	0.5

3.4 Energy dissipation evaluation

Energy monitoring was achieved by post processing the files output during the simulations. These files contained wall stress values and positions, and particle contact forces, velocities and positions, which were used to calculate the various energy terms. Equation (2.13) was used to determine the energy changes.

From Equation (2.13), the total change in dissipated energy, ΔE_η can be derived as the sum of the changes in frictional dissipation, damping dissipation, and bonding energy. For simulations in the present chapter, bonding energy was zero. Since the simulations had particles at low velocity values, it was found that the potential and kinetic energies were each $\approx 10^6$ times smaller than either of the boundary work or the stored elastic energy. The total change in dissipated energy, ΔE_η was therefore approximated for all simulations to be the difference between change in boundary work and change in strain energy based on equation (2.13) as

$$\Delta E_\eta \approxeq \Delta W - \Delta E_s \tag{3.2}$$

where the boundary work is given by

$$\Delta W = \sigma_z A_S \delta z, \tag{3.3}$$

and δz is the constant distance change of the top mesh, which for this study was calculated from the

output files in the post-procession stage for every 0.0025 simulation seconds to reduce the computational cost. A_S is the surface area for the bottom platen mesh, and σ_z is the average normal stress on that mesh.

Changes in the stored energy are due to the evolution of both the magnitude of the forces through contacts. The summation of strain energy for all the contacts is equal to the stored energy and was obtained using

$$\begin{aligned} \Delta E_s &= \Delta E_s^n + \Delta E_s^t, \\ \Delta E_s^n &= | \underbrace{\overbrace{\frac{4}{3} E^* \sqrt{R^* \delta_n}}^{K_n} \delta_n \mathbf{n}}_{F^n} | \, d_n \text{ and} \\ \Delta E_s^t &= | \underbrace{\overbrace{8 G^* \sqrt{R^* \delta_n}}^{K_t} \xi_t}_{F^t} | \, d\xi_t, \end{aligned} \tag{3.4}$$

where ΔE_s^n and ΔE_s^t are the contributions from normal and tangential contact forces respectively. F^n and F^t are in turn the normal and tangential contact forces and K_n and K_t are the corresponding stiffness parameters using the Hertzian contact model, which governs how spherical particles interact at contacts. d_n is the normal displacement. Two particles A and B in contact will have an effective radius, $R^* = R_A R_B/(R_A + R_B)$, which is the geometric mean of radii R_A and R_B. $\delta_n = R_A + R_B - d_{AB}$ is the overlap at contact between the two particles in the normal direction where d_{AB} is the distance between their centres. The effective Young's modulus, $E^* = 0.5E/(1-\nu^2)$ since the particles are of the same material, and is derived from the particles' material Young's modulus, E and Poisson's ratio, ν. In Equation (3.4), $\boldsymbol{n}$ is a normal vector for particles in contact. The term ξ_t in (3.4) is the tangential displacement calculated by integrating the tangential relative velocity v_t over the contact time; that is, $\xi_t = \int_{t_0} v_t dt$ [139].

3.5 Results and discussion

Minh and Cheng [140] observed that the compression of granular assemblies is due to the rearrangement of particles and elastic compression. Figure 3.2 shows the state of a typical simulation sample at the start of loading and at the end of the loading and unloading cycles. A horizontal reference line is drawn over these states. A comparison of the top of the sample states with the horizontal line shows that the unloading state has a lower top surface than the top. This is because samples experienced unrecoverable rearrangement during the loading cycle. This leads to particles generating locked in stresses that are not released in the unloading cycle. Furthermore, the unrecoverable rearrangement helps to explain the different paths followed by the loading and unloading cycles as represented in the e-log(σ_v) graphs in Figures 3.3-3.5, where the outermost curves for each set of data are the loading cycle and the innermost are the unloading cycle.

Figure 3.3 shows the results based on the first row values in Table 3.1 in which the circled part highlights an area where the pressure dropped during two of the simulations. This was caused by a sudden rearrangement within the specimens with $C_u = 1$ and $C_u = 1.3$ due to pockets of voids being filled rapidly.

Figure 3.4 shows the results of the second row in Table 3.1 at different μ values. The variations between the loading and unloading cycles for different μ values are not significant. The main reason for this is that changes in void ratio are largely due to the densifying of the particles, a process that is mainly

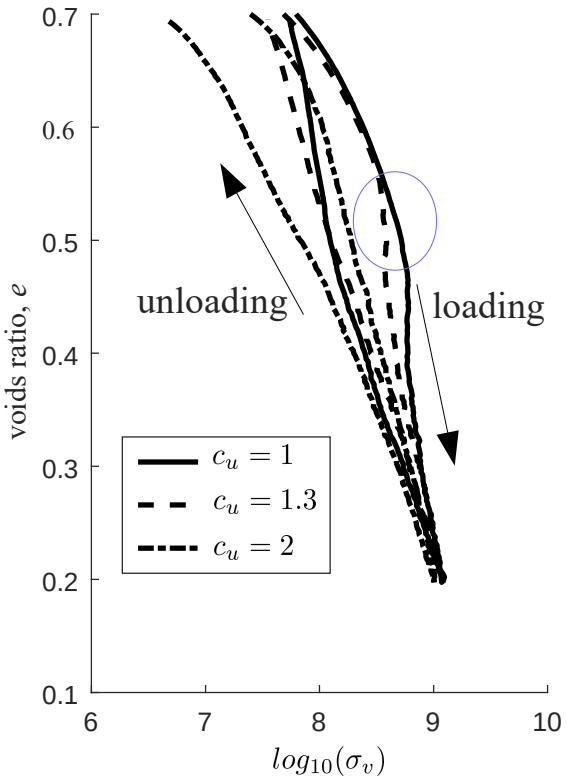

Figure 3.3: e-logσ_v results for different C_u values

governed by the movement of the top platen.

Figure 3.5 shows the results for the loading and unloading cycles at ten different initial void ratios (e_{ini}) from $0.7 - 0.43$ (see Table 3.1). A similar compression path was followed towards the end of the loading cycle as would be expected. The slight differences correspond to the oscillations of particles during the simulations. The unloading path also follows a similar path for all the ten simulations. The loading compression lines all converge to the same point with the same slope which agrees with experimental observations (for example, [17, 141]).

The permanent rearrangement of the particles in the samples is also reflected in the energy dissipation graphs in Figures 3.6-3.8. Here energy dissipation is presented normalised per unit solid volume. The data is plotted against the axial strain. The loading cycle follows the bottom part of each curve from 0 to 30% strain except for results in Figure 3.8 where the initial void ratio is considered, since the lowest void ratio reached was kept the same for all simulations. After the loading cycle, the unloading cycle moves from right to left. The loading cycle contributed most to the cumulative energy dissipated.

It can be seen from these energy graphs that the magnitude of the change in energy dissipation during loading is slightly higher than during unloading. This is further confirmation of the fact that there is less particle rearrangement on the unloading cycle due to the unrecoverable locked in stress within the sample gained on the loading cycle.

Permanent deformation of soils has been observed in experimental result like subgrade soils under pavement due to repeated loading [142], and in sand due to cyclic loading [143].

The results in energy dissipation graphs indicate that a higher C_u results in less energy dissipation as shown in Figure 3.6. This observation may be explained as follows. As smaller particles are introduced, voids can easily be filled during the loading cycle and therefore less energy is dissipated since there is less particle rearrangement. This result suggests that the cumulative energy dissipation for these simulations

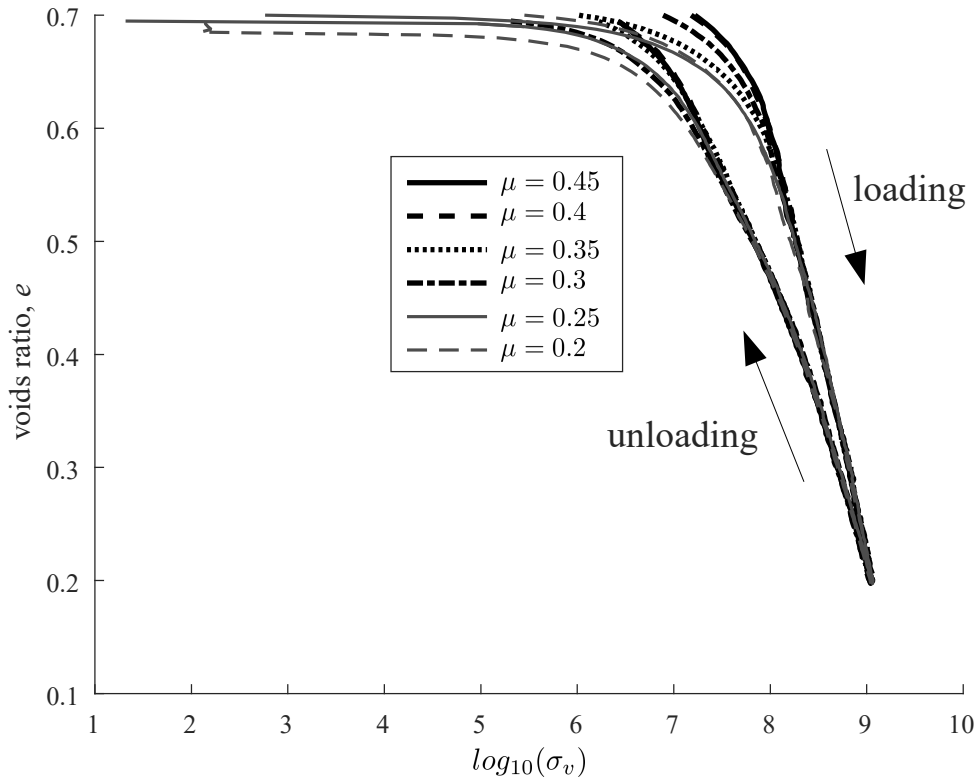

Figure 3.4: e-logσ_v results for different μ values

is negatively correlated to the coefficient of uniformity.

A higher inter-particle coefficient of friction results in more energy dissipation during loading and unloading as observed in Figure 3.7 for Simulations 4-9 (Table 3.1). This observation is consistent with the fact that energy is largely lost through friction. The cumulative energy dissipation is therefore expected to be positively correlated with the inter-particle coefficient of friction.

Figure 3.8 shows that the energy dissipation loading curves become steeper with a decreasing initial void ratios, e_{ini}. This is because more input energy is required to move particles through the same strain increment due to higher stresses in the contacts most of which is dissipated. There is also a similar gradient achieved at a higher strain levels for samples with a higher e_{ini}. More energy is dissipated on unloading as the e_{ini} decreases. A physical explanation to this can be obtained by first observing that a low initial void ratio corresponds to a denser sample. More energy is required to move particles in a denser sample since they are more resistant to sliding. As particles slide to allow compression, energy is dissipated. These observations suggest that the cumulative energy dissipation is negatively correlated with the initial void ratio.

To assess the state of the fabric, the average coordination number was calculated as

$$Z = \frac{N_c}{N_p} \tag{3.5}$$

where N_c is the number of contacts and N_p is the number of particles. The coordination number is a simple particle scale parameter that measures the packing density or packing intensity [1]. Figures 3.9-3.11 show the variation of this number over time for different C_u, μ, and e_{ini} values. A lower C_u

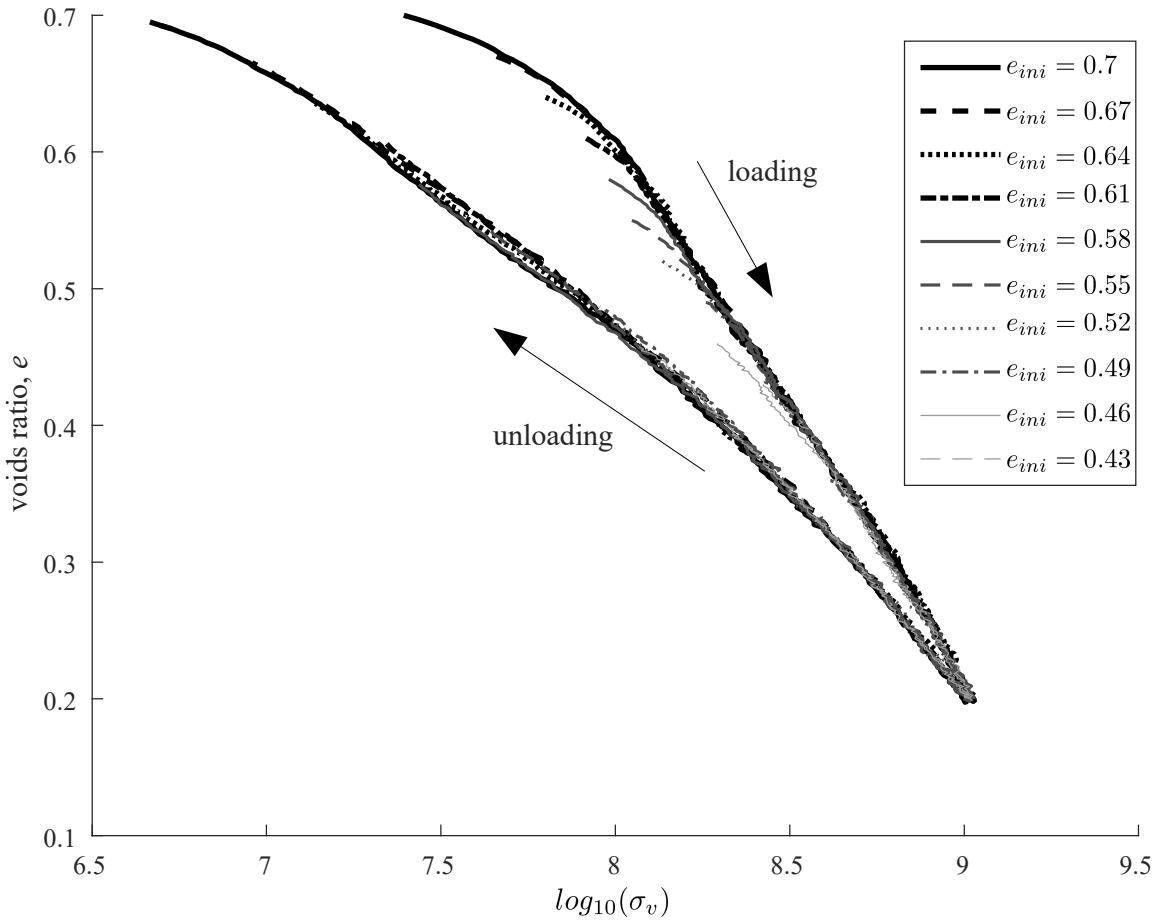

Figure 3.5: e-logσ_v results for different e_{ini} values

leads to a higher coordination number as loading progresses as seen in Figure 3.9. This is because larger particles have larger surfaces and can, therefore, have multiple contacts. Smaller particles introduced into the sample have less contacts, which in turn reduces the average coordination number. The increase in Z with a decrease in C_u can further help to explain the results in Figure 3.6. More contacts mean that particles can lose more energy through sliding due to increased surfaces of contact and higher forces in these contacts.

Varying the inter particle coefficient of friction shows that lower μ values lead to a higher average coordination numbers as the loading cycle progresses (Figure 3.10). The reason for this is the fact that a lower friction coefficient leads to less resistance to sliding resulting in more particle contacts. Although this means that there are more contacts, it does not result in more energy dissipation as shown in Figure 3.7. This is perhaps due to the fact that the differences in coordination number are small and therefore the inter particle coefficient of friction has a more dominate effect over energy dissipation.

Figure 3.11 shows that the coordination number variation over time is less affected by the initial void ratio since the same value is reached at the end of loading where the void ratio is the same for all simulations.

Figure 3.12 shows an example of the resultant particle force vectors for simulation with $e_{ini} = 0.7$, $\mu = 0.5$, and $C_u = 1$. The arrows plot the direction vector while the colouring indicates magnitude. It can be seen from the Figure that there is an overall increase in the internal force when comparing the start of loading (a) and the end of loading (b). This helps explain the increase in energy dissipation as

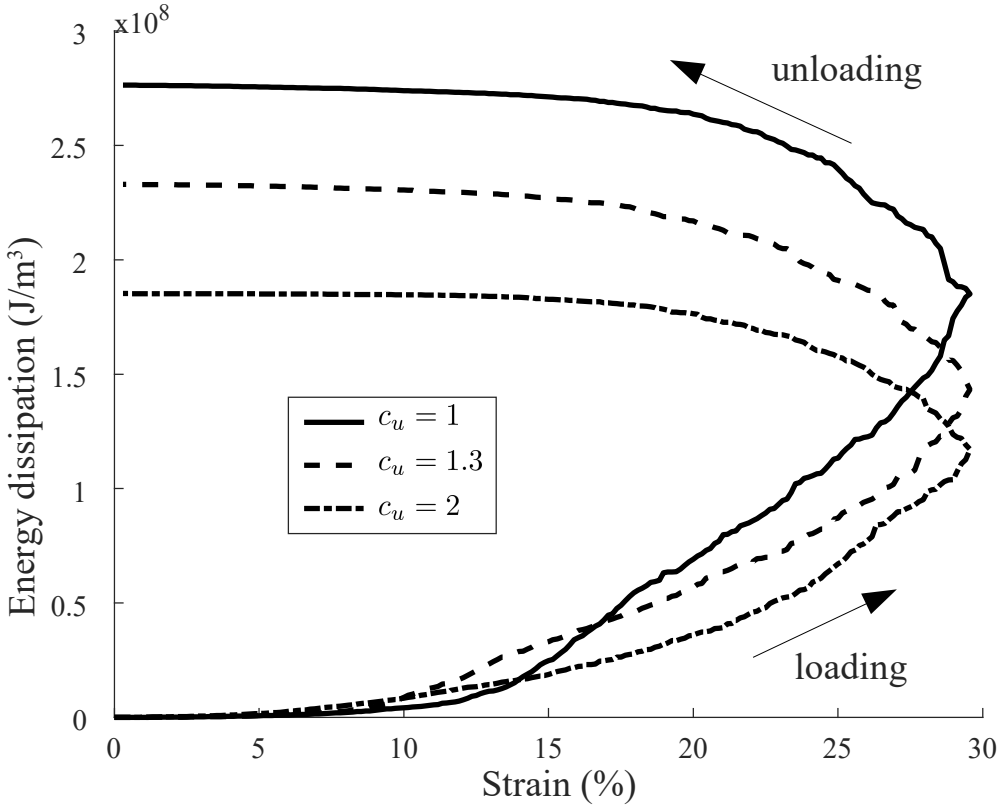

Figure 3.6: Dissipated energy against strain results for different C_u values

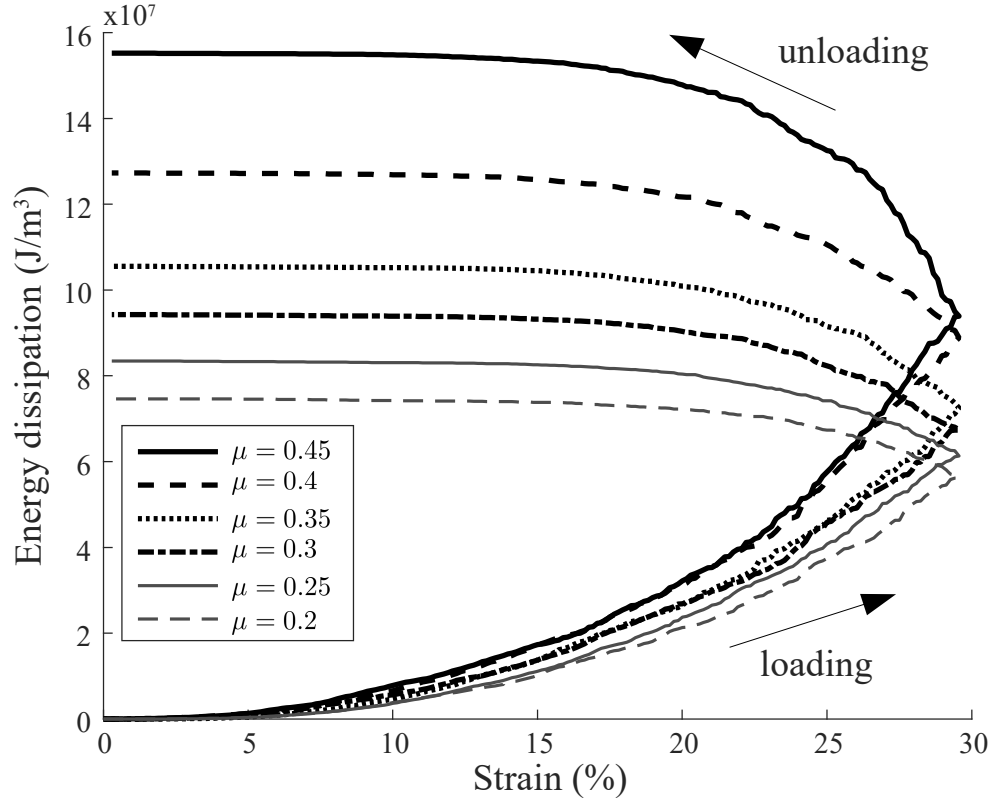

Figure 3.7: Dissipated energy against strain results for different μ values

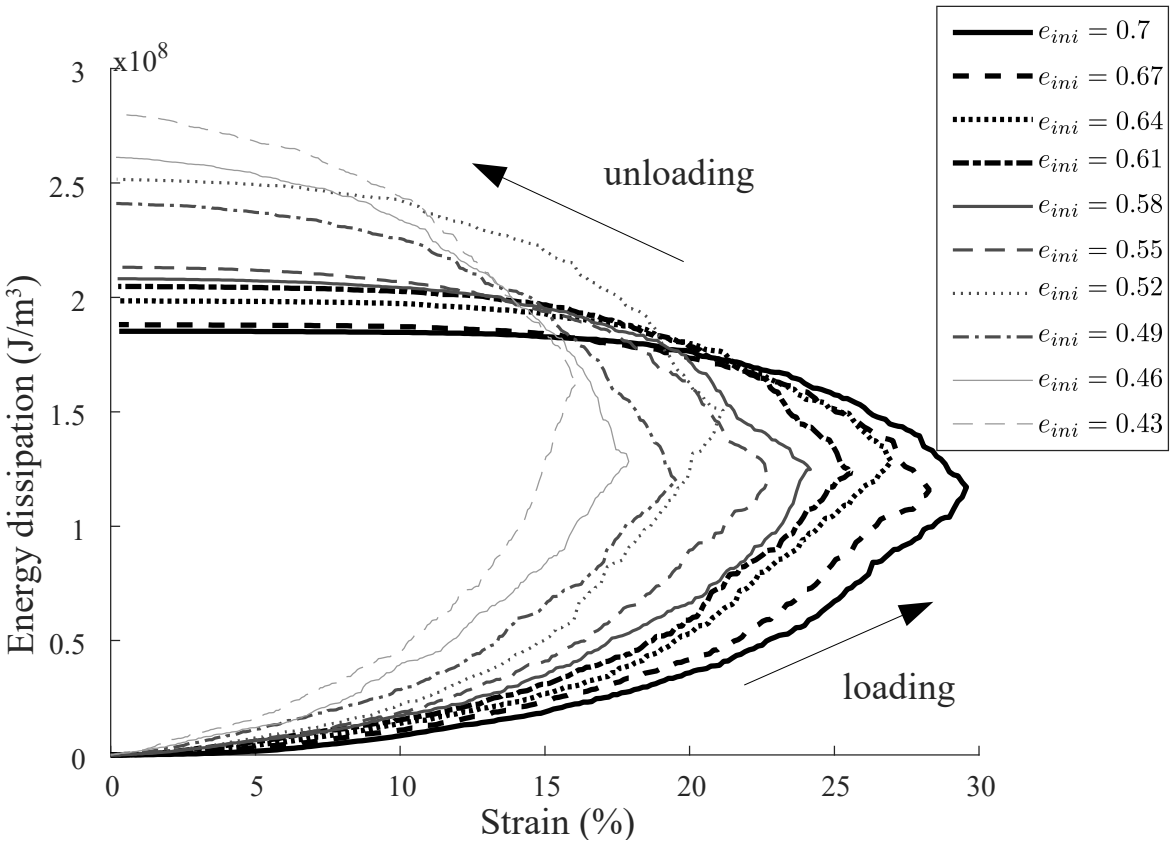

Figure 3.8: Dissipated energy against strain results for different e_{ini} values

loading progresses. The force magnitude has a large concentration in the sample centre, which is because the wall reactions tend to push the particles inwards. A preference of the particle force towards the right side in Figure 3.12(b) for this particular simulation was as a result of the large localised movement of particles at the early stages of loading stage that led to a concentration of particles to one side of the sample. Figure 3.12 does show that there was no strong directional preference for the resultant force vectors.

3.6 Observations

One-dimensional compression tests using the DEM have been conducted through loading and unloading cycles using spherical particles whose elastic properties were set to those of sands. PSD, initial voids ratio, and the coefficient of friction were the three parameters varied in the present new study of their influence on energy dissipation in one-dimensional normal compression DEM tests. Increasing the coefficient of uniformity was found to decrease the energy dissipated; lowering the initial voids ratio resulted in steeper curves for energy dissipation; and a higher inter-particle coefficient of friction resulted in more energy dissipation. The average coordination number during the loading and unloading cycles supports the observations from the coefficient of uniformity results. It was also observed that the inter particle coefficient of friction had a more dominating effect on energy dissipation than the average coordination number for the simulations presented in this chapter. It is important to note, however, that the simulations in this chapter were carried out using small samples, which were not representative element volumes potentially resulting in significant effect from bounding walls. A variation in the initial stress or initial void ratio between samples, leading to differences in initial states, could limit some of the observations made.

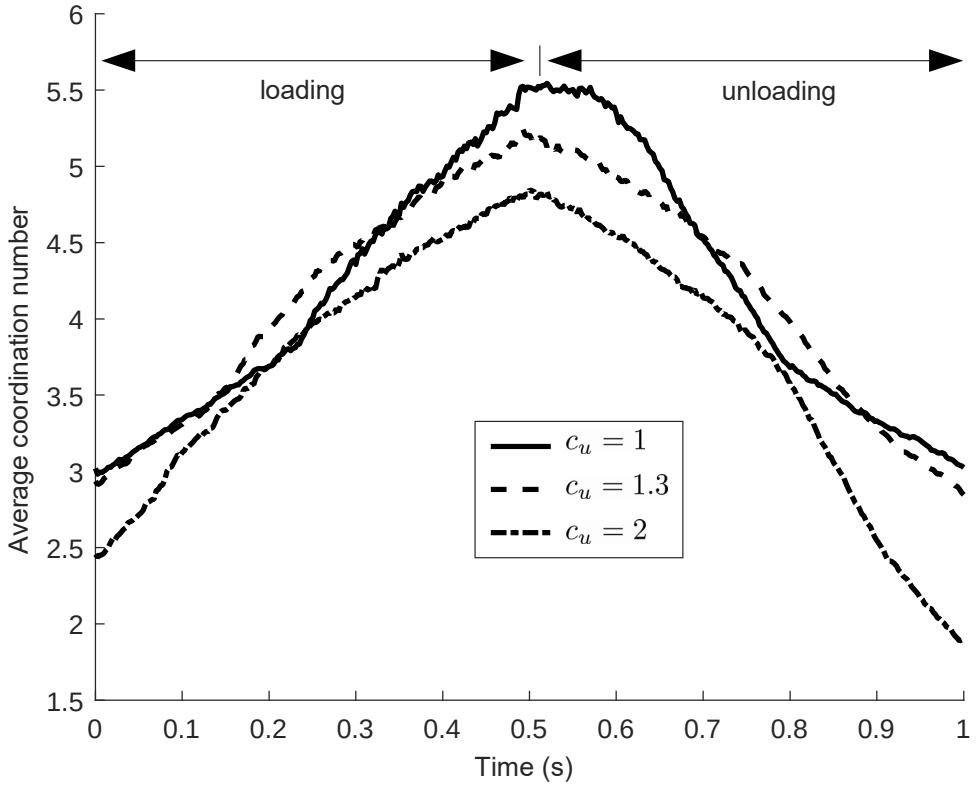

Figure 3.9: Average coordination number over time for different C_u values

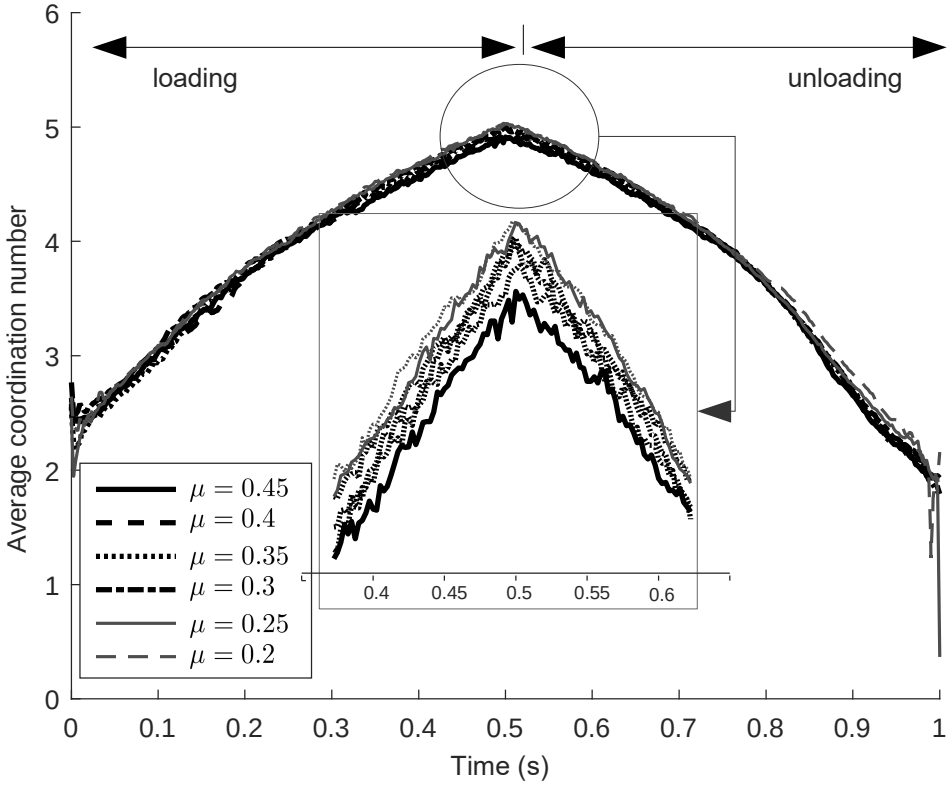

Figure 3.10: Average coordination number over time for different μ values

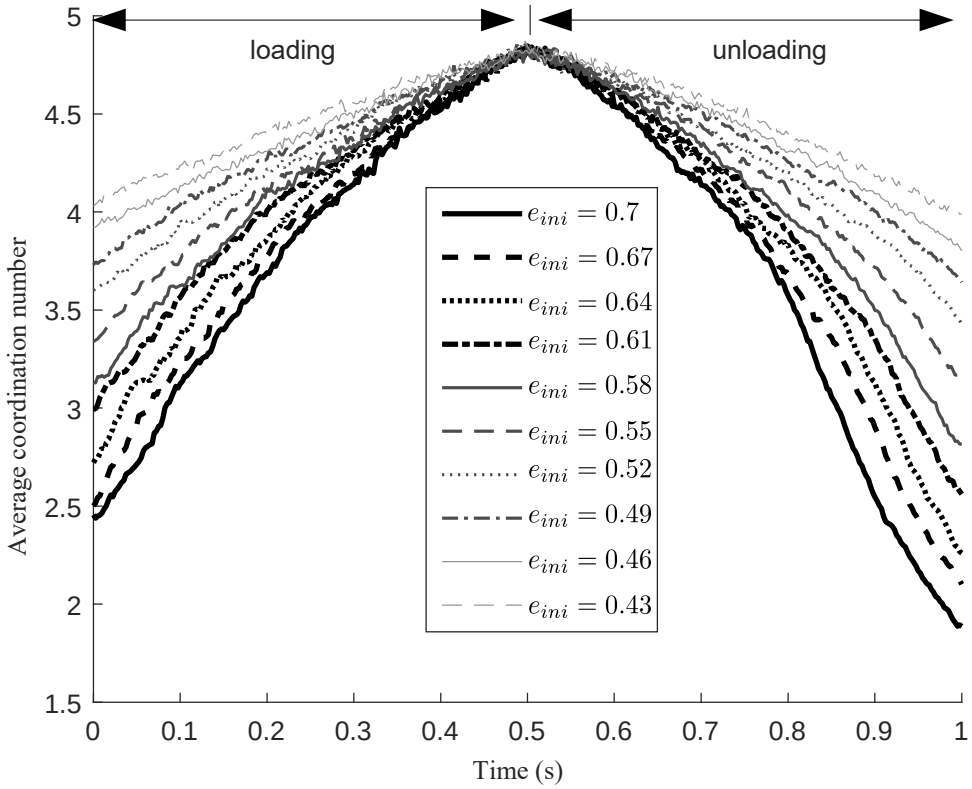

Figure 3.11: Average coordination number over time for different e_{ini} values

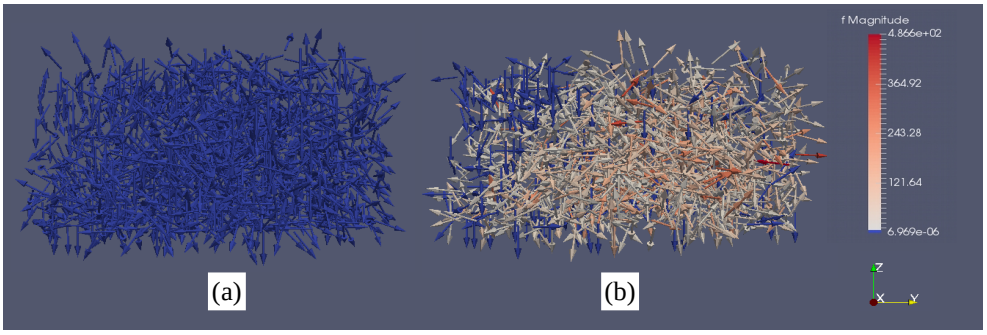

Figure 3.12: Snapshot of the resultant force: (a) at the start of loading; and (b) at the end of loading

Chapter 4

Conclusions

Chapter 1 introduced the thesis by highlighting how the DEM can facilitate a study of granular media by modelling individual grains to derive a rich understanding of their behaviour. It was established that using DEM to study energy dissipation can lead to the construction of constitutive models using the hyperplasticity approach. It was pointed out that the thesis itself focussed only on understanding of energy dissipation from a DEM perspective.

Chapter 2 discussed the DEM model and provided a literature review of the DEM application. It showed how DEM can capture physically hard to measure parameters.

The novel research in the thesis is described in Chapter 3 where the influence of Particle size distribution, initial void ratio, and the coefficient of friction on energy dissipation in one-dimensional normal compression DEM test simulations were studied. It is envisioned that the findings can help inform the formulation of continuum functions linking energy dissipation to grain scale parameters.

As discussed in Chapter 3, increasing the coefficient of uniformity was found to decrease the energy dissipated due to the fact that smaller particles are introduced, which reduce the sliding of particles while increasing the amount of stored energy. A lower initial void ratio resulted in steeper curves for energy dissipation due to the fact that more input energy was required to move the particles through the same displacement at lower initial void ratio values most of which was dissipated. A higher friction coefficient between particles resulted in more energy dissipation during loading and unloading of the samples due to the fact that energy is mainly lost through friction, which is directly proportional to its coefficient.

4.1 Recommendations and future work

The one-dimensional normal compression tests can be extended to three dimensional loading conditions such as are found in triaxial tests. Energy dissipation studies can then be done and energy dissipation rates established from the results. These rates can then be used to formulate constitutive models.

A repetition of the simulations presented under difference boundary conditions, with controlled consistent initial states, and all samples having more particles such that they can be representative element volumes would be recommended to observe whether similar results can be obtained.

References

[1] C. O'Sullivan, *Particulate Discrete Element ModeModel: A Geomechanics Perspective*, vol. 4. Routledge, 2013.

[2] M. Jiang, J. Konrad, and S. Leroueliil, "An efficient technique for grenerating homogeneous specimens for DEM studies," *Computer and Geotechnics*, vol. 30, pp. 579–597, 2003.

[3] J. Sykut, M. Molenda, and J. Horabik, "Discrete element method (DEM) as a tool for investigating properties of granular materials," *Polish journal of food and nutrition sciences*, vol. 57, pp. 169–173, 2007.

[4] Z. Zhang, L. Liu, Y. Yuan, and A. Yu, "A simulation study of the effects of dynamic variables on the packing of spheres," *Powder Technology*, vol. 116, no. 1, pp. 23–32, 2001.

[5] R. Davis and A. Selvadurai, *Plasticity and Geomechanics*. Cambridge University Press, 2002.

[6] P. A. Cundall and O. D. L. Strack, "A discrete numerical model for granular assemblies," *Géotechnique*, vol. 29, pp. 47–65, 1979.

[7] P. Cundall and R. Hart, "Numerical modelling of discontinua," *Engineering Computations*, vol. 9, pp. 101–113, 1992.

[8] C. Abbireddy and C. Clayton, "The impact of particle form on the packing and shear behaviour of some granular materials: an experimental study," *Granular Matter*, vol. 17, no. 4, pp. 427–438, 2015.

[9] P. Cundall and O. D. L. Strack, "The development of constitutive laws for soils using the distinct element method," in *Numerical methods in geomechanics*, no. 1, pp. 289–317, 1979.

[10] J. Rodriguez-Ortiz, *Estudio del Comportamiento de Medios Granulares Heterogeneos Mediante Modelos Discontinuos Analógicos y Matemáticos*. PhD thesis, Universidad Politecnica de Madrid, 1974.

[11] G. De Josselin de Jong and A. Verruijt, "Etude photo-elastique d'un empilement de disques," *Cahiers du Groupe français de rhéologie*, vol. 1, pp. 73–86, 1969.

[12] F. Bertrand, L.-A. Leclaire, and G. Levecque, "DEM-based models for the mixing of granular materials," *Chemical Engineering Science*, vol. 60, no. 8, pp. 2517–2531, 2005. 5th International Symposium on Mixing in Industrial Processes (ISMIP5).

[13] G. Houlsby and A. Puzrin, *Principles of Hyperplasticity*. Springer, 2006.

[14] H. Ziegler, *An introduction to thermomechanics*. North Holland Pub. Co, Amsterdam, 2nd ed., 1983.

[15] G. Houlsby, *A Study of Plasticity Theories and Their Applicability to Soils*. PhD thesis, University of Cambridge, 1981.

[16] M. O. Ciantia, M. Arroyo, F. Calvetti, and A. Gens, "An approach to enhance efficiency of dem modelling of soils with crushable grains," *Géotechnique*, vol. 65, no. 2, pp. 91–110, 2015.

[17] Y. Nakata, Y. Kato, M. Hyodo, A. Hyde, and H. Murata, "One-dimensional compression behaviour of uniformly graded sand related to single particle crushing strength," *Soils and Foundations*, vol. 41, no. 2, pp. 39–51, 2001.

[18] G. Mesri and B. Vardhanabhuti, "Compression of granular materials," *Canadian Geotechnical Journal*, vol. 46, no. 4, pp. 369–392, 2009.

[19] G. McDowell and J. de Bono, "On the micro mechanics of one-dimensional normal compression," *Géotechnique*, vol. 3, pp. 166–172, 2013.

[20] *DEM-Solutions - https://www.altair.com/edem/*. Last Accessed 31 March 2022.

[21] *Newton - https://www.demsoftware.net/*. Last Accessed 31 March 2022.

[22] *ESyS-Particle - https://launchpad.net/esys-particle*. Last Accessed 31 March 2022.

[23] ITASCA Consulting Group, Inc., *PFC - http://www.itascacg.com/software/pfc*. Last Accessed 20 Aug 2015.

[24] CFDEM project, *LIGGGHTS Open Source Discrete Element Method particle simulation code - https://www.cfdem.com/*. Last Accessed 31 March 2022.

[25] C. Kloss, C. Goniva, A. Hager, S. Amberger, and S. Pirker, "Models, algorithms and validation for opensource DEM and CFD-DEM," *Progress in Computational Fluid Dynamics, An Int. J.*, vol. 12, pp. 140–152, 2012.

[26] G. Sutmann, "Classical molecular dynamics," *Quantum Simulations of Complex Many-Body Systems: From Theory to Algorithms - Lecture Notes*, vol. 10, pp. 211–254, 2002. John von Neumann Institute for Computing, Jülich, NIC Series.

[27] H. Kinloch and C. O'Sullivan, "A micro-mechanical study of the influence of penetrometer geometry on failure mechanisms in granular soils," in *Advances in Measurement and Modeling of Soil Behavior*, pp. 1–11, 2007.

[28] G. Marketos and M. D. Bolton, "Flat boundaries and their effect on sand testing," *International Journal for numerical and analytical methods in geomechanics*, vol. 34, no. 8, pp. 821–837, 2010.

[29] S. K. Chan and K. M. Ng, "Geometrical characteristics of a computer-generated three-dimensional packed column of equal and unequal sized spheres—with special reference to wall effects," *Chemical Engineering Communications*, vol. 48, no. 4-6, pp. 215–236, 1986.

[30] B. Hardin, "Effect of rigid boundaries on measurement of particle concentration," *Geotechnical Testing Journal*, vol. 12, no. 2, pp. 143–149, 1989.

[31] P. A. Cundall, "Computer simulations of dense sphere assemblies," in *Studies in Applied Mechanics* (M. Satake and J. Jenkins, eds.), vol. 20, pp. 113–123, Elsevier, 1988.

[32] Y. H. Wang and S. C. Leung, "A particle-scale investigation of cemented sand behavior," *Candian Geotechnical Journal*, vol. 45, no. 1, pp. 29–44, 2008.

[33] J. P. De Bono, G. R. McDowell, and D. Wanatowski, "Discrete element modelling of a flexible membrane for triaxial testing of granular material at high pressures," *Géotechnique Letters*, vol. 2, no. 4, pp. 199–203, 2012.

[34] W. Powrie, Q. Ni, R. M. Harkness, and X. Zhang, "Numerical modelling of plane strain tests on sands using a particulate approach," *Géotechnique*, vol. 55, no. 4, pp. 297–306, 2005.

[35] G. Cheung and C. O'Sullivan, "Effective simulation of flexible lateral boundaries in two-and three-dimensional dem simulations," *Particuology*, vol. 6, no. 6, pp. 483–500, 2008.

[36] L. Cui, C. O'sullivan, and S. O'neill, "An analysis of the triaxial apparatus using a mixed boundary three-dimensional discrete element model," *Géotechnique*, vol. 57, no. 10, pp. 831–844, 2007.

[37] J. A. Ferrez, *Dynamic Triangulations for Efficient 3-D simulation of Granular Materials*. PhD thesis, Ecole Polytechnique Federal de Lausanne, 2001.

[38] D. O. Potyondy and P. A. Cundall, "A bonded-particle model for rock," *International Journal of Rock Mechanics and Mining Sciences*, vol. 41, no. 8, pp. 1329–1364, 2004.

[39] N. H. Minh, Y. P. Cheng, and C. Thornton, "Strong force networks in granular mixtures," *Granular Matter*, vol. 16, no. 1, pp. 69–78, 2014.

[40] K. Bagi, "An algorithm to generate random dense arrangements for discrete element simulations of granular assemblies," *Granular Matter*, vol. 7, pp. 31–43, 2005.

[41] C. Abbiready and C. R. I. Clayton, "Varying initial void rratio for DEM simulations," *Géotechnique*, vol. 60, no. 6, pp. 497–502, 2010.

[42] M. O. Ciantia, K. Boschi, T. Shire, and S. Emam, "Numerical techniques for fast generation of large discrete-element models," *Proceedings of the Institution of Civil Engineers - Engineering and Computational Mechanics*, vol. 171, no. 4, pp. 147–161, 2018.

[43] G. Delaney, S. Inagaki, and T. Aste, "Fine tuning dem simulations to perform virtual experiments with three-dimensional granular packings," in *Granular and Complex Materials*, pp. 169–185, World Scientific, 2007.

[44] H. Hertz, "Über die Berührung fester elastischer Körper," *Journal für die reine und angewandte Mathematik*, vol. 92, pp. 156–171, 1881.

[45] R. Mindlin and H. Deresiewicz, "Elastic spheres in contact under varying oblique forceforce," *ASME Journal of Applied Mechanics*, vol. 20, pp. 327–344, 1953.

[46] K. Johnson, "One hundred years of hertz contact," *Proceedings of the Institution of Mechanical Engineers*, vol. 196, no. 1, pp. 363–378, 1982.

[47] O. Walton and R. Braun, "Viscosity, granular-temperature, and stress calculations for shearing assemblies of inelastic, frictional disks," *Journal of rheology*, vol. 30, no. 5, pp. 949–980, 1986.

[48] Y. Ye and Y. Zeng, "A size-dependent viscoelastic normal contact model for particle collision," *International Journal of Impact Engineering*, vol. 106, pp. 120–132, 2017.

[49] C. Thornton, S. Cummins, and P. Cleary, "On elastic-plastic normal contact force models, with and without adhesion," *Powder Technology*, vol. 315, pp. 339–346, 2017.

[50] L. Vu-Quoc and X. Zhang, "An accurate and efficient tangential force–displacement model for elastic frictional contact in particle-flow simulations," *Mechanics of materials*, vol. 31, no. 4, pp. 235–269, 1999.

[51] A. Di Renzo and F. Di Maio, "Comparison of contact-force models for the simulation of collisions in DEM-based granular flow codes," *Chemical engineering science*, vol. 59, no. 3, pp. 525–541, 2004.

[52] C. Thornton and K. Yin, "Impact of elastic spheres with and without adhesion," *Powder technology*, vol. 65, no. 1-3, pp. 153–166, 1991.

[53] A. Munjiza and K. Andrews, "NBS contact detection algorithm for bodies of similar size," *International Journal for Numerical Methods in Engineering*, vol. 43, no. 1, pp. 131–149, 1998.

[54] J.-F. Ferellec and G. McDowell, "A method to model realistic particle shape and inertia in DEM," *Granular Matter*, vol. 12, no. 5, pp. 459–467, 2010.

[55] M. Purvance, D. Russell, D. Potyondy, and S. Emam, "Spatial searching and contact detection in PFC 5.0," in *Continuum and Distinct Element Numerical Modeling in Geomechanics: 2011 : Proceedings of the 2nd International FLAC/DEM Symposium, Melbourne, Australia, February 14-16, 2011*, ITASCA Consulting Group, 2011.

[56] K. Han, Y. Feng, and D. Owen, "Performance comparisons of tree-based and cell-based contact detection algorithms," *Engineering Computations*, vol. 24, no. 2, pp. 165–181, 2007.

[57] B. Vemuri, L. Chen, L. Vu-Quoc, X. Zhang, and O. Walton, "Efficient and accurate collision detection for granular flow simulation," *Graphical models and image processing*, vol. 60, no. 6, pp. 403–422, 1998.

[58] Y. Feng and D. Owen, "An augmented spatial digital tree algorithm for contact detection in computational mechanics," *International Journal for Numerical Methods in Engineering*, vol. 55, no. 2, pp. 159–176, 2002.

[59] D. Eppstein, M. Goodrich, and J. Sun, "Skip quadtrees: Dynamic data structures for multidimensional point sets," *International Journal of Computational Geometry & Applications*, vol. 18, no. 1-2, pp. 131–160, 2008.

[60] C. O'Sullivan and J. Bray, "Selecting a suitable time-step for discrete element simulations that use the central difference time integration approach," *Engineering Computations*, vol. 21, no. 2-4, pp. 278–303, 2003.

[61] H. Zhu, Z. Zhou, R. Yang, and A. Yu, "Discrete particle simulation of particulate systems: Theoretical developments," *Chemical Engineering Science*, vol. 62, pp. 3378–3396, 2007.

[62] C. O'Sullivan, "Advancing geomechanics using DEM," *Geomechanics from Micro to Macro*, pp. 21–32, 2014.

[63] H. Zhu, Z. Zhou, R. Yang, and A. Yu, "Discrete particle simulation of particulate systems: A review of major applications and findings," *Chemical Engineering Science*, vol. 63, pp. 5728–5770, 2008.

[64] H. Tangri, Y. Guo, and J. Curtis, "Packing of cylindrical particles: DEM simulations and experimental measurements," *Powder Technology*, vol. 317, pp. 72–82, 2017.

[65] C. Martin, "Unloading of powder compacts and their resulting tensile strength," *Acta Materialia*, vol. 51, no. 15, pp. 4589–4602, 2003.

[66] C. Martin and D. Bouvard, "Study of the cold compaction of composite powders by the discrete element method," *Acta Materialia*, vol. 51, no. 2, pp. 373–386, 2003.

[67] C. Martin, D. Bouvard, and S. Shima, "Study of particle rearrangement during powder compaction by the discrete element method," *Journal of the Mechanics and Physics of Solids*, vol. 51, no. 4, pp. 667–693, 2003.

[68] C. Martin, D. Bouvard, and G. Delette, "Discrete element simulations of the compaction of aggregated ceramic powders," *Journal of the American Ceramic Society*, vol. 89, no. 11, pp. 3379–3387, 2006.

[69] Y. Cheng, Y. Nakata, and M. Bolton, "Discrete element simulation of crushable soil," *Géotechnique*, vol. 53, no. 7, pp. 633–641, 2003.

[70] M. Ciantia, C. O'Sullivan, and R. J. Jardine, "Pile penetration in crushable soils: Insights from micromechanical modelling," in *17th European Conference on soil Mechanics and Geotechnical Engineering (ECSMGE 2019)*, International Society for Soil Mechanics and Geotechnical Engineering, 2019.

[71] D. Potyondy and P. Cundall, "A bonded-particle model for rock," *International Journal of Rock Mechanics and Mining Sciences*, vol. 48, no. 8, pp. 1329–1364, 2004.

[72] C. O'Sullivan, J. Bray, and L. Cui, "Experimental validation of particle-based discrete element methods," 2006.

[73] C. O'Sullivan, L. Cui, and S. O'Neil, "Discrete element analysis of the response of granular materials during cyclic loading," *Soils and Foundations*, vol. 48, pp. 511–530, 2008.

[74] F. Alonso-Marroquin, H. B. Muhlhaus, and H. J. Herrmann, "Micromechanical investigation of granular ratcheting using a discrete model of polygonal particles," *Particuology*, vol. 6, pp. 390–403, 2008.

[75] C. Thornton, "Numerical simulations of deviatoric shear deformation of granular media," *Géotechnique*, vol. 50, no. 1, pp. 43–53, 2000.

[76] D. Barreto and C. O'Sullivan, "The influence of interparticle friction and the intermediate stress ratio on soil response under generalised stress conditions," *Granular Matter*, vol. 14, no. 4, pp. 505–521, 2012.

[77] C. O'Sullivan, J. Bray, and S. Li, "A new approach for calculating strain for particulate media," *International Journal for Numerical and Analytical Methods in Geomechanics*, vol. 27, no. 10, pp. 859–877, 2003.

[78] S. Li and H. Yu, "Influence of loading direction on the behavior of anisotropic granular materials," *International Journal of Engineering Science*, vol. 47, pp. 1284–1296, 2009.

[79] S. Yimsiri and K. Soga, "DEM analysis of soil fabric effects on behaviour of sand," *Géotechnique*, vol. 60, no. 6, pp. 483–495, 2010.

[80] D. Kang, T. Yun, Y. Lau, and Y. Wang, "DEM simulation on soil creep and associated evolution of pore characteristics.," *Computers and Geotechnics*, vol. 39, pp. 98–106, January 2012.

[81] L. Cui and C. O'Sullivan, "Exploring the macro-and micro-scale response of an idealised granular material in the direct shear apparatus," *Géotechnique*, vol. 56, no. 7, pp. 455–468, 2006.

[82] L. Zhang and C. Thornton, "A numerical examination of the direct shear test," *Géotechnique*, vol. 57, no. 4, pp. 343–354, 2007.

[83] J. Wang, M. Gutierrez, and J. Dove, "Numerical studies of shear banding in interface shear tests using a new strain calculation method," *International Journal for Numerical and Analytical Methods in Geomechanics*, vol. 31, no. 12, pp. 1349–1366, 2007.

[84] M. Bernhardt, G. Biscontin, and C. O'Sullivan, "Experimental validation study of 3D direct simple shear DEM simulations," *Soils and Foundations*, vol. 56, no. 3, pp. 336–347, 2016.

[85] M. Asadzadeh and A. Soroush, "Fundamental investigation of constant stress simple shear test using DEM," *Powder Technology*, vol. 292, pp. 129–139, 2016.

[86] M. Asadzadeh and A. Soroush, "Macro-and micromechanical evaluation of cyclic simple shear test by discrete element method," *Particuology*, vol. 31, pp. 129–139, 2017.

[87] M. R. Kuhn, "Structured deformation in granular materials," *Mechanics of materials*, vol. 31, no. 6, pp. 407–429, 1999.

[88] C. O'Sullivan, J. Bray, and M. Riemer, "Influence of particle shape and surface friction variability on response of rod-shaped particulate media," *Journal of Engineering Mechanics*, vol. 128, no. 11, pp. 1182–1192, 2002.

[89] S. Luding, "Shear flow modeling of cohesive and frictional fine powder," *Powder Technology*, vol. 158, no. 1-3, pp. 45–50, 2005.

[90] S. Luding, "Anisotropy in cohesive, frictional granular media," *Journal of Physics: Condensed Matter*, vol. 17, no. 24, p. S2623, 2005.

[91] D. Kang, T. Yun, and T. Evans, "Pore orientation of granular materials during biaxial compression," *Computers and Geotechnics*, vol. 59, pp. 1–11, 2014.

[92] C. O'Sullivan, J. Bray, and M. Riemer, "Examination of the response of regularly packed specimens of spherical particles using physical tests and discrete element simulations," *Journal of engineering mechanics*, vol. 130, no. 10, pp. 1140–1150, 2004.

[93] J. de Bono, G. McDowell, and D. Wanatowski, "Discrete element modelling of a flexible membrane for triaxial testing of granular material at high pressures," *Géotechnique Letters*, vol. 2, pp. 199–203, 2012.

[94] J. P. De Bono and G. R. McDowell, "DEM of triaxial tests on crushable sand," *Granular Matter*, vol. 16, pp. 551–562, 2014.

[95] X. Wang and J. Li, "Simulation of triaxial response of granular materials by modified DEM," *Science China Physics, Mechanics & Astronomy*, vol. 57, no. 12, pp. 2297–2308, 2014.

[96] K. Hanley, X. Huang, and C. O'Sullivan, "Energy dissipation in soil samples during drained triaxial shearing," *Géotechnique*, vol. 68, no. 5, pp. 421–433, 2017.

[97] S. Luding, M. Lätzel, W. Volk, S. Diebels, and H. Herrmann, "From discrete element simulations to a continuum model," *Computer methods in applied mechanics and engineering*, vol. 191, no. 1-2, pp. 21–28, 2001.

[98] S. Lobo-Guerrero and L. Vallejo, "Modeling granular crushing in ring shear tests: experimental and numerical analyses," *Soils and Foundations*, vol. 46, no. 2, pp. 147–157, 2006.

[99] P. Langston, M. Nikitidis, U. Ttiztin, D. Heyes, and N. Spyrou, "Microstructural simulation and imaging of granular flows in two- and three-dimensional hoppers," *Powder Technology*, vol. 94, pp. 59–72, 1997.

[100] J. Landry, G. Grest, and S. Plimpton, "Discrete element simulations of stress distributions in silos: crossover from two to three dimensions," *Powder Technology*, vol. 139, pp. 233–239, 2004.

[101] C. S. Campbell, P. W. Cleary, and M. A. Hopkins, "Large scale landslide simulations: global deformation, velocities and basal friction," *Journal of Geophysical Research*, vol. 100, pp. 8267–8283, 1995.

[102] P. W. Cleary, "DEM simulation of industrial particle flows: case studies of dragline excavators, mixing in tumblers and centrifugal mills," *Powder Technology*, vol. 109, pp. 83–104, 2000.

[103] O. Pekau and C. Yuzhu, "Failure analysis of fractured dams during earthquakes by dem," *Engineering Structures*, vol. 26, pp. 1483–1502, 2004.

[104] J. Zhao and T. Shan, "Coupled CFD–DEM simulation of fluid–particle interaction in geomechanics," *Powder Technology*, vol. 239, pp. 248–258, 2013.

[105] P. Rowe, "The stress-dilatancy relation for static equilibrium of an assembly of particles in contact," *Proceedings of the Royal Society of London. Series A, Mathematical and Physical Sciences*, vol. 269, no. 1339, pp. 500–527., 1962.

[106] J. O'Donovan, *Micromechanics of Wave Propagation through Granular Material*. Ph. d. thesis, Imperial College London, 2014.

[107] G. Houlsby, T. Zhao, and S. Utili, "3D DEM investigation of granular column collapse: Evaluation of debris motion and its destructive power," *Engineering Geology*, vol. 186, pp. 3–16, February 2015.

[108] B. N. Asmar, P. A. Langston, A. J. Matchett, and J. K. Walters, "Energy monitoring in distinct element models of particle systems," *Advanced Powder Technology*, vol. 14, no. 1, pp. 43–69, 2003.

[109] J. Wang and H. Yan, "DEM analysis of energy dissipation in crushable soils," *Soils and Foundations*, vol. 52, pp. 644–657, August 2012.

[110] R. Hurley, J. Lind, D. Pagan, M. Akin, and E. Herbold, "In situ grain fracture mechanics during uniaxial compaction of granular solids," *Journal of the Mechanics and Physics of Solids*, vol. 112, pp. 273–290, 2018.

[111] P. Wang and C. Arson, "Energy distribution during the quasi-static confined comminution of granular materials," *Acta Geotechnica*, pp. 1–9, 2018.

[112] N. Zhang, M. Arroyo, M. O. Ciantia, A. Gens, and J. Butlanska, "Standard penetration testing in a virtual calibration chamber," *Computers and Geotechnics*, vol. 111, pp. 277–289, 2019.

[113] W. Zhang, J. Wang, and M. Jiang, "DEM-Aided discovery of the relationship between energy dissipation and shear band formation considering the effects of particle rolling resistance," *Journal of Geotechnical and Geoenvironmental Engineering*, vol. 139, pp. 1512–1527, 2013.

[114] J. Kozicki, J. Tejchman, and Z. Mróz, "Effect of grain roughness on strength, volume changes, elastic and dissipated energies during quasi-static homogeneous triaxial compression using DEM," *Granular Matter*, vol. 12, pp. 457–468, 2012.

[115] X. Li and Y. Dafalias, "Dissipation consistent fabric tensor definition from DEM to continuum for granular media," *Journal of the Mechanics and Physics of Solids*, vol. 78, pp. 141–153, 2015.

[116] U. Shamy and C. Denissen, "Microscale characterization of energy dissipation mechanisms in liquefiable granular soils," *Computers and Geotechnics*, vol. 37, pp. 846–857, 2010.

[117] D. Daudon, P. Villard, V. Richefeu, and G. Mollon, "Influence of the morphology of slope and blocks on the energy dissipations in a rock avalanche," *Mechanics of granular and polycrystalline solids*, vol. 343, no. 2, pp. 166–177, 2015.

[118] M. O. Ciantia, M. Arroyo, F. Calvetti, and A. Gens, "A numerical investigation of the incremental behavior of crushable granular soils," *International Journal for Numerical and Analytical Methods in Geomechanics*, vol. 40, no. 13, pp. 1773–1798, 2016.

[119] F. Calvetti, G. Viggiani, C. Tamagnini, *et al.*, "A numerical investigation of the incremental behavior of granular soils," *Rivista italiana di geotecnica*, vol. 37, no. 3, pp. 11–29, 2003.

[120] A. Britto and M. Gunn, *Critical state soil mechanics via finite elements*. Ellis Horwood, 1987.

[121] M. Bolton, Y. Nakata, and Y. P. Cheng, "Micro- and macro-mechanical behaviour of DEM crushable materials," *Géotechnique*, vol. 58, no. 6, pp. 471–480, 2008.

[122] L. Tong and Y.-H. Wang, "DEM simulations on the energy dissipation in soil under static and cyclic loading," *Proceedings of the Fifth International Symposium on Deformation Characteristics of Geomaterials, IS-Seoul*, pp. 614–619, 2011.

[123] R. Kondner and M. Ho, "Energy dissipation of a cohesive soil by the fourier transformation of stress relaxation response," *Transactions Of The Society Of Rheology*, vol. 6, no. 1, pp. 145–157, 1965.

[124] S. Utili and R. Nova, "DEM analysis of bonded granular geomaterials," *Int. J. Numer. Anal. Meth. Geomech.*, vol. 32, pp. 1997–2031, 2008.

[125] T. Tsuji, Y. Nakagawa, N. Matsumoto, Y. Kadono, T. Takayama, and T. Tanaka, "3-D DEM simulation of cohesive soil-pushing behavior by bulldozer blade," *Journal of Terramechanics*, vol. 49, no. 1, pp. 37–47, 2012.

[126] R. Moreno-Atanasio, "Energy dissipation in agglomerates during normal impact," *Powder Technology*, vol. 223, pp. 12–18, 2012.

[127] J. Wang and H. Yan, "3D DEM Simulation of crushable granular soils under plane strain compression condition," *Procedia Engineering*, vol. 14, pp. 1713–1720, 2011.

[128] N. Estrada, E. Azéma, F. Radjai, and A. Taboada, "Identification of rolling resistance as a shape parameter in sheared granular media," *Physical Review E*, vol. 84, p. p011306, July 2011.

[129] K. Mao, M. Wang, Z.X., and T. Chen, "DEM simulation of particle damping," *Powder Technology*, vol. 142, no. 2-3, pp. 154–165, 2004.

[130] L. Tong, *DEM simulations of energy dissipation in sand and dynamic properties.* MPhil, Hong Kong University of Science and Technology, 2012.

[131] Y.-J. Lin and K.-S. Hwang, "Effects of particle size and particle size distribution on heat dissipation of heat pipes with sintered porous wicks," *Metallurgical and Materials Transactions A*, vol. 40, no. 9, pp. 2071–2078, 2009.

[132] J. Kozicki, J. Tejchman, and H. Ḿtuhlhaus, "Discrete simulations of a triaxial compression test for sand by DEM," *Journal for Numerical and Analytical Methods in Geomechanics*, vol. 38, pp. 1923–1952, 2014.

[133] H. McNamara, "An estimate of energy dissipation due to soil-moisture hysteresis," *Water Resources Research*, vol. 50, no. 1, pp. 725–735, 2014.

[134] *ParaView - https://www.paraview.org/.* Last Accessed 31 March 2022.

[135] J. F. Wang and R. Huang, "DEM study on energy allocation behavior in crushable soils," *Advanced Materials Research*, vol. 871, pp. 119–123, December 2013.

[136] N. P. Daphalapurkar, F. Wang, B. Fu, and R. Komanduri, "Determination of mechanical properties of sand grains by nanoindentation," vol. 51, pp. 719–728, 2011.

[137] J. P. De Bono and G. R. McDowell, "Discrete element modelling of one-dimensional compression of cemented sand," *Granular Matter*, vol. 16, pp. 79–90, 2014.

[138] D. Muir Wood and K. Maeda, "Changing grading of soil: effect on critical states," *Acta Geotechnica.*

[139] X. Dou, Y. Mao, and Y. Zhang, "Effects of contact force model and size distribution on microsized granular packing," *J. Manuf. Sci. Eng*, vol. 136, no. 2, p. 021003, 2014.

[140] N. H. Minh and Y. P. Cheng, "A DEM investigation of the effect of particle-size distribution on one-dimensional compression," *Géotechnique*, vol. 63, pp. 44–53, 2013.

[141] G. McDowell, "On the yielding and plastic compression of sand," *Soils and foundations*, vol. 42, no. 1, pp. 139–145, 2002.

[142] A. J. Puppala, S. Saride, and S. Chomtid, "Experimental and modeling studies of permanent strains of subgrade soils," *Journal of geotechnical and geoenvironmental engineering*, vol. 135, no. 10, pp. 1379–1389, 2009.

[143] C. S. Chang and R. V. Whitman, "Drained permanent deformation of sand due to cyclic loading," *Journal of geotechnical engineering*, vol. 114, no. 10, pp. 1164–1180, 1988.